A multifluid Taylor-Galerkin methodology for the simulation of compressible multicomponent separate two-phase flows from subcritical to supercritical states

Milan Pelletier, Schmitt Thomas, Sebastien Ducruix

▶ **To cite this version:**

Milan Pelletier, Schmitt Thomas, Sebastien Ducruix. A multifluid Taylor-Galerkin methodology for the simulation of compressible multicomponent separate two-phase flows from subcritical to supercritical states. Computers and Fluids, 2020, 206, pp.104588. 10.1016/j.compfluid.2020.104588 . hal-03049812

HAL Id: hal-03049812
https://hal.science/hal-03049812v1

Submitted on 10 Dec 2020

HAL is a multi-disciplinary open access archive for the deposit and dissemination of scientific research documents, whether they are published or not. The documents may come from teaching and research institutions in France or abroad, or from public or private research centers.

L'archive ouverte pluridisciplinaire **HAL**, est destinée au dépôt et à la diffusion de documents scientifiques de niveau recherche, publiés ou non, émanant des établissements d'enseignement et de recherche français ou étrangers, des laboratoires publics ou privés.

A multifluid Taylor-Galerkin methodology for the simulation of compressible multicomponent separate two-phase flows from subcritical to supercritical states

Milan Pelletier, Thomas Schmitt*, Sébastien Ducruix

Laboratoire EM2C, CNRS, Ecole CentraleSupélec, Université Paris-Saclay, 3 rue Joliot-Curie 91192 Gif-sur-Yvette, France

Abstract

In various industrial combustion devices, such as liquid rocket engines at ignition or Diesel engines during the compression stage, the operating point varies over a wide range of pressures. These pressure variations can lead to a change of thermodynamic regime when the critical pressure is exceeded, switching from two-phase injection to transcritical injection. Such change modifies the topology of the flow and the mixing, thereby impacting the flame dynamics. This motivates the development of a unified methodology able to address both subcritical and supercritical flows within the same solver. To achieve this, the present work provides an extension of the supercritical real gas Taylor-Galerkin solver AVBP-RG to subcritical two-phase flows, based on diffuse interface models. In particular, the required developments for the integration of a multifluid model into the finite-element framework of this solver are detailed. Then, the ability of the solver to address a subcritical configuration is tested by simulating two subcritical-pressure operating points (G1 at 4.7 MPa and A10 at 1 MPa) of the MASCOTTE test bench operated by ONERA. This allows to confront the model with experimental data, showing good agreement.

Keywords: Two-phase Flow, Supercritical Flow, Non-Ideal Thermodynamics, Multifluid Methods, Multicomponent Two-Phase Equilibrium

*Corresponding author
Email address: thomas.schmitt@centralesupelec.fr (Thomas Schmitt)

1. Introduction

For many internal combustion engines, e.g. liquid rocket engines during ignition, the chamber pressure can drastically vary. As a consequence, thermodynamic states that can range from subcritical to supercritical conditions are likely to occur, and the transition from one regime to the other may be observed. The objective of the present work is to propose a framework that is able to simulate compressible flows ranging from subcritical to supercritical states.

The modeling of supercritical injection and combustion has been and still is the object of a sustained research effort [1, 2, 3, 4]. A key point is the modeling of non-ideal *real-gas* effects that are classically addressed by using cubic Equations of States (EoS), such as the Peng-Robinson or the Soave Redlich Kwong EoS [5, 6]. These thermodynamic closures have been deeply studied and prove to be relevant for supercritical *large-eddy simulations* (LES) [7, 8], as done in particular within the Taylor-Galerkin LES solver AVBP-RG [9, 10, 11]. The present work is based on the AVBP-RG solver and presents the developments required to handle subcritical flows in it.

In the subcritical domain, single-phase states can become unstable, leading to phase separation. The instability can be mechanical or chemical (in the case of multicomponent mixtures), corresponding respectively to a loss of thermodynamic convexity along the pressure direction or along the chemical composition directions. In this case, models are needed to address the liquid-gas interfaces and the atomization processes. For the modeling of separate two-phase flows, the existing interface modeling strategies can be split into two major families: *sharp interface methods* and *diffuse interface methods*. The first one describes the interface as an infinitely thin surface separating liquid and gas phases, across which the fluid properties are discontinuous. Different strategies are then studied to transport and handle the interface, either by capturing it for instance the *level-set* methods [12, 13, 14] or the *volume-of-fluid* methods [15, 16] or by tracking it, as done by the *front-tracking* methods [17, 18]. Such methods

are really promising, in particular for the simulation of two-phase flows in an incompressible context. In the case of compressible flows, as targeted by the present work, these methods often suffer from mass and energy conservation issues [19, 20]. For compressible cases, the strategies encountered in the literature mostly focus on the second family of methods, *diffuse interface methods*. Also, these methods seem more adapted to handle the interface appearance and disappearance that can occur in the targeted applications. Within this framework, the interface consists in a diffuse region between pure phases. On the one hand, this region can be physically determined, as for the *phase-field* methods such as the *second-gradient theory* [21, 22], which are not yet able to handle compressible flows in industrial configurations. On the other hand, the interface can be described by an artificially diffused region that is used to model the interface behaviour, as done by the *multifluid methods* [23, 24, 25, 26, 27]. These methods rely on an ensemble averaging of the phases properties to formulate sets of equations that rule the two-phase flow evolution, which are hyperbolic provided that convex thermodynamic closures are used [28]. In this framework, the assumption of pressure, temperature and chemical potentials equilibria between phases yields simplified multifluid models that involve only conservative equations to describe the evolution of the two-phase flow, which is convenient to treat numerically [27, 29]. These latter papers consider convex *stiffened-gas* EoS to model the phases thermodynamics. The present work extends their use to cubic EoS.

It is worth mentioning that the community of Diesel injection research recently explored analogous pathways [30, 31, 32, 33], and lately came to the LRE application, tackling the question of water condensation suspected to occur at high-pressure operating points [34]. These latter works use classic finite-volume solvers for models that relate to the equilibrium multifluid ones. In particular, they rely on cubic EoS with multicomponent two-phase equilibrium computations that involve either costly iterative methods or case-specific tabulations.

The present work proposes (i) an implementation of the equilibrium multifluid models within a low-dissipation finite element Taylor-Galerkin LES solver

and (ii) a computationally efficient approximate multicomponent two-phase equilibrium formulation. Applications to the simulation of the Mascotte G1 [35] and A10 [36] configurations at 1 MPa (subcritical regime regarding pure O_2) are proposed, in order to evaluate this strategy on a realistic subcritical case. It is worth mentioning that in this first approach, considering the high Weber and Reynolds number that characterize the considered cases, the surface tension is neglected.

The paper is structured as follows. Section 2 focuses on the multifluid models and their implementation within a Taylor-Galerkin numerical framework. Section 3 discusses the thermodynamic closures used. Section 4 proposes 1D validation test cases for the developed framework. Then, Section 5 presents the integration of the multifluid models within the LES solver. Finally, Section 6 is dedicated to the analysis of the simulation results obtained on the Mascotte configurations.

2. Taylor-Galerkin formulation of the multifluid models

2.1. The Taylor-Galerkin numerical framework

The Taylor-Galerkin methods were initially introduced in [37], to solve typical hyperbolic conservative transport equations which read:

$$\frac{\partial \mathbf{U}}{\partial t} + \vec{\nabla} \cdot \vec{\mathcal{F}}\left(\mathbf{U}\right) = 0, \tag{1}$$

with $\mathbf{U}$ the conservative variables and $\vec{\mathcal{F}}\left(\mathbf{U}\right)$ the corresponding flux. Among this class of methods [38], the family of *two-step Taylor-Galerkin* (TTG) methods has been studied by [39], providing computationally efficient third-order low-dissipation schemes, such as the $\mathbb{P}^1$ TTGC and TTG4A methods. They can be written under the following form:

$$\mathcal{M}\tilde{\mathbf{U}}^n = \mathcal{M}\mathbf{U}^n - \alpha_{\mathrm{TTG}}\Delta t \boldsymbol{\mathcal{T}} \cdot \vec{\mathbf{F}}^n + \beta_{\mathrm{TTG}}\Delta t^2 \boldsymbol{\mathcal{D}} : \boldsymbol{\mathcal{J}}^n \cdot \vec{\mathbf{F}}^n \tag{2a}$$

$$\begin{aligned}\mathcal{M}\mathbf{U}^{n+1} = \mathcal{M}\mathbf{U}^n &- \Delta t \left(\theta_{\mathrm{TTG}} \boldsymbol{\mathcal{T}} \cdot \vec{\mathbf{F}}^n + \tilde{\theta}_{\mathrm{TTG}} \boldsymbol{\mathcal{T}} \cdot \tilde{\vec{\mathbf{F}}}^n\right) \\ &+ \Delta t^2 \left(\varepsilon_{\mathrm{TTG}}\Delta t^2 \boldsymbol{\mathcal{D}} : \boldsymbol{\mathcal{J}}^n \cdot \vec{\mathbf{F}}^n + \tilde{\varepsilon}_{\mathrm{TTG}} \boldsymbol{\mathcal{D}} : \tilde{\boldsymbol{\mathcal{J}}}^n \cdot \tilde{\vec{\mathbf{F}}}^n\right).\end{aligned} \tag{2b}$$

Here, $\mathbf{U}^n$, $\tilde{\mathbf{U}}^n$ and $\mathbf{U}^{n+1}$ are respectively the vector of conservative variables at time t^n, at the intermediate step and at the next time step. The fluxes are given by $\vec{\mathbf{F}}^n = \vec{\mathcal{F}}(\mathbf{U}^n)$ and $\tilde{\vec{\mathbf{F}}}^n = \vec{\mathcal{F}}(\tilde{\mathbf{U}}^n)$. $\mathcal{J}^n$ and $\tilde{\mathcal{J}}^n$ correspond to the Jacobian matrix of the flux function. The coefficients α_{TTG}, β_{TTG}, θ_{TTG}, $\tilde{\theta}_{\mathrm{TTG}}$, $\varepsilon_{\mathrm{TTG}}$ and $\tilde{\varepsilon}_{\mathrm{TTG}}$ are constant parameters of the TTG method. The operators $\mathfrak{M}$, $\boldsymbol{\mathcal{T}}$ and $\mathfrak{D}$ are respectively the Galerkin mass tensor, the advection tensor and the diffusion tensor, which are constant for a given mesh.

Here, it is important to notice the presence of the Jacobian matrix of the flux function $\mathcal{J}$. This matrix has to be determined, in particular in the case of the multifluid methods considered. The following sections present the considered multifluid models and the computation of the corresponding Jacobian matrix.

2.2. The 3-equation model

The basic idea to be explored in the present work for solving subcritical flows is to extend the use of the PR or SRK cubic EoS to subcritical states. These EoS are known to lose their local convexity in the region of thermodynamic instability, and their global convexity in the region of thermodynamic metastability. The proposed strategy is to restore the convexity by considering phase change in these regions. Phase changes are then addressed by assuming the fluid mixture to be in thermodynamic equilibrium. This strategy corresponds to a 3-equation multifluid method [40].

2.2.1. Model formulation

In this section, for the sake of clarity, the one-dimensional case is considered. Formally, the 3-equation model has the same formulation as the Euler equations:

$$\frac{\partial \mathbf{U}}{\partial t} + \frac{\partial \mathcal{F}(\mathbf{U})}{\partial x} = 0, \tag{3}$$

with

$$\mathbf{U} = \begin{bmatrix} \rho Y_1 \\ \vdots \\ \rho Y_{N_s} \\ \rho u \\ \rho e_{\mathrm{t}} \end{bmatrix} \qquad \text{and} \qquad \mathcal{F}(\mathbf{U}) = \begin{bmatrix} \rho Y_1 u \\ \vdots \\ \rho Y_{N_s} u \\ \rho u^2 + P \\ (\rho e_{\mathrm{t}} + P)u \end{bmatrix}. \tag{4}$$

Here, ρ denotes the mixture density, $Y_k = \frac{m_k}{m}$ the mass fraction of species k, u the flow velocity, P the pressure, $e_{\mathrm{t}} = e_s + e_k$ the mass-specific total energy, with e_s the sensible energy and $e_k = \frac{1}{2}u^2$ the kinetic energy.

From this model, two regimes may then be encountered: if the single-phase solution is thermodynamically stable (pure liquid or pure gas), then the thermodynamic closure is directly given by the cubic EoS. Otherwise, if the single-phase solution is not thermodynamically stable, the eventually obtained state corresponds to a two-phase mixture, so that the transported density and volume-specific sensible energy correspond to mixture properties. This reads

$$\begin{cases} \rho = z_\ell \rho_\ell^{\mathrm{sat}} + (1 - z_\ell)\rho_v^{\mathrm{sat}}, & \text{(5a)} \\ \rho e_s = z_\ell \rho_\ell^{\mathrm{sat}} e_\ell^{\mathrm{sat}} + (1 - z_\ell)\rho_v^{\mathrm{sat}} e_v^{\mathrm{sat}}, & \text{(5b)} \end{cases}$$

where z_ℓ is the liquid volume fraction. The phases properties at saturation are here denoted with the superscript "sat", which will be omitted in the rest of the paper for the sake of simplicity. The system is closed by the following equilibrium conditions:

$$\begin{cases} P^\ell = P^v, & \text{(6a)} \\ T^\ell = T^v, & \text{(6b)} \\ g_i^\ell = g_i^v, \ \forall i \in [\![1, N_s]\!], & \text{(6c)} \end{cases}$$

with indices ℓ and v denoting respectively the liquid and the vapour phase properties, and g_i^ϕ the partial Gibbs energy of species i in phase $\phi \in \{\ell, v\}$ – or, equivalently, the chemical potential.

2.2.2. Jacobian terms

The Jacobian matrix for the 3-equation model can be written, for any thermodynamic closure, as follows:

$$\mathcal{J}(\mathbf{U}) = \begin{bmatrix} (1-Y_1)u & \cdots & -Y_{N_s}u & Y_1 & 0 \\ \vdots & \ddots & \vdots & \vdots & \vdots \\ -Y_1 u & \cdots & \big(1-Y_{N_s}\big)u & Y_{N_s} & 0 \\ -u^2+\zeta(e_c-\xi_1) & \cdots & -u^2+\zeta\big(e_c-\xi_{N_s}\big) & (2-\zeta)u & \zeta \\ \big[(e_c-\xi_1)\zeta-h_\mathrm{t}\big]u & \cdots & \Big[\big(e_c-\xi_{N_s}\big)\zeta-h_\mathrm{t}\Big]u & h_\mathrm{t}-u^2\zeta & (1+\zeta)u \end{bmatrix}, \tag{7}$$

with h_t the total enthalpy and $e_c = \frac{u^2}{2}$ the mass-specific kinetic energy. In this formulation, the thermodynamic closure is contained in the differential coefficients ζ and $(\xi_i)_{i\in[\![1,N_s]\!]}$, defined as

$$\zeta = \left.\frac{\partial P}{\partial \rho e_s}\right|_{\rho,\underline{\boldsymbol{Y}}}, \tag{8a}$$

$$\xi_i = \left.\frac{\partial \rho e_s}{\partial \rho Y_i}\right|_{P,\rho Y_{j\neq i}}. \tag{8b}$$

In the single-phase case, these coefficients [41] reduce to:

$$\zeta = \frac{\alpha}{\rho\beta c_\mathrm{v}}, \tag{9a}$$

$$\xi_i = \frac{\rho c_\mathrm{p}}{\alpha} v_i - h_{s,i}, \tag{9b}$$

with α and β respectively the isobaric thermal expansion and the isothermal compressibility coefficients, c_v and c_p respectively the isochoric and isobaric specific heat capacities, v_i the partial specific volume of species i and $h_{s,i}$ the partial specific enthalpy of species i.

The evaluation of ζ and ξ_i in the two-phase case requires to compute the variations of the flow properties along the two-phase thermodynamic equilibrium, which will be detailed in Section 3.

Also, the 3-equation model having the same structure as the Euler equations, the speed of sound is classically given by

$$c^2 = \left.\frac{\partial P}{\partial \rho}\right|_{s,\underline{\boldsymbol{Y}}}. \tag{10}$$

In the one-phase case, it is given by

$$c^2 = \frac{c_\mathrm{p}}{\rho\beta c_\mathrm{v}} \tag{11}$$

In the two-phase case, the entropy s and density ρ are mixture properties. The derivation of the two-phase speed of sound will be given in Section 3.

2.2.3. Boundary conditions

The boundary conditions are applied using the characteristic formalism developed in [42]. Their formulation involves transformation matrices that contain the coefficients ζ and ξ_i, and the speed of sound c. The transformation matrices used to apply the boundary conditions are provided in Appendix C.

2.3. The 4-equation model

An alternative strategy that can be used to compute the transport assuming phase equilibrium consists in using the 4-equation model [40, 43]:

$$\frac{\partial \mathbf{U}}{\partial t} + \frac{\partial \mathcal{F}\left(\mathbf{U}\right)}{\partial x} = \mathcal{S}(\mathbf{U}), \tag{12}$$

where the conservative variables, the flux function and the phase change source terms are defined as:

$$\mathbf{U} = \begin{bmatrix} \rho Y_1^\ell \\ \vdots \\ \rho Y_{N_s}^\ell \\ \rho Y_1^v \\ \vdots \\ \rho Y_{N_s}^v \\ \rho u \\ \rho e_\mathrm{t} \end{bmatrix}, \ \mathcal{F}\left(\mathbf{U}\right) = \begin{bmatrix} \rho Y_1^\ell u \\ \vdots \\ \rho Y_{N_s}^\ell u \\ \rho Y_1^v u \\ \vdots \\ \rho Y_{N_s}^v u \\ \rho u^2 + P \\ (\rho e_\mathrm{t} + P)u \end{bmatrix}, \text{ and } \mathcal{S}\left(\mathbf{U}\right) = \begin{bmatrix} \kappa_1(g_1^\ell - g_1^v) \\ \vdots \\ \kappa_{N_s}(g_{N_s}^\ell - g_{N_s}^v) \\ -\kappa_1(g_1^\ell - g_1^v) \\ \vdots \\ -\kappa_{N_s}(g_{N_s}^\ell - g_{N_s}^v) \\ 0 \\ 0 \end{bmatrix}. \tag{13}$$

Here, the phase-wise species mass fractions $\left(Y_i^\phi\right)_{\phi\in\{\ell,v\},i\in[\![1,N_s]\!]}$ are defined as $Y_i^\phi = \frac{m_i^\phi}{m_i}$ with m_i^ϕ the mass of the i^{th} component in phase ϕ and m_i the mass

of the i^{th} component across both phases, so that $Y_i^v + Y_i^\ell = Y_i$. The quantities κ_i appearing in the source terms correspond to relaxation coefficients.

Assuming infinitely fast relaxation towards phase equilibrium, which reads

$$\forall i, \kappa_i \to +\infty, \tag{14}$$

an operator-splitting strategy can be used [29, 43, 44] in order to solve the homogeneous equilibrium transport. This can be summarized as follows:

(i) To compute the 4-equation hyperbolic transport, which assumes only pressure and temperature equilibrium, without accounting for the source terms

(ii) To compute the phase equilibrium corresponding to the obtained variables $\rho, \rho u, \rho e_{\text{t}}$ and the species mass fractions $Y_i = Y_i^v + Y_i^\ell$

In order to apply such a strategy within the Taylor-Galerkin numerical framework, the Jacobian terms for the hyperbolic transport step (i) of the 4-equation model shall be provided. One can show that the following form is obtained for any thermodynamic closure:

$$\mathcal{J}(\mathbf{U}) = \begin{bmatrix} (1-Y_1^\ell)u & \cdots & -Y_{N_s}^\ell u & -Y_1^v u & \cdots & -Y_{N_s}^v u & Y_1^\ell & 0 \\ \vdots & \ddots & \vdots & \vdots & \ddots & \vdots & \vdots & \vdots \\ -Y_1^\ell u & \cdots & (1-Y_{N_s}^\ell)u & -Y_1^v u & \cdots & -Y_{N_s}^v u & Y_{N_s}^\ell & 0 \\ -Y_1^\ell u & \cdots & -Y_{N_s}^\ell u & (1-Y_1^v)u & \cdots & -Y_{N_s}^v u & Y_1^v & 0 \\ \vdots & \ddots & \vdots & \vdots & \ddots & \vdots & \vdots & \vdots \\ -Y_1^\ell u & \cdots & -Y_{N_s}^\ell u & -Y_1^v u & \cdots & (1-Y_{N_s}^v)u & Y_{N_s}^v & 0 \\ A_1^\ell & \cdots & A_{N_s}^\ell & A_1^v & \cdots & A_{N_s}^v & (2-\zeta)u & \zeta \\ B_1^\ell & \cdots & B_{N_s}^\ell & B_1^v & \cdots & B_{N_s}^v & h_{\text{t}}-u^2\zeta & (1+\zeta)u \end{bmatrix}, \tag{15}$$

with the following terms:

$$A_i^\phi = -u^2 + \zeta\left(e_c - \xi_i^\phi\right) \tag{16}$$

$$B_i^\phi = \left[\left(e_c - \xi_i^\phi\right)\zeta - h_{\text{t}}\right]u \tag{17}$$

Here, the differential coefficients $(\xi_i^\phi)_{\phi\in\{\ell,v\},i\in[\![1,N_s]\!]}$ and ζ are defined as

$$\zeta = \left.\frac{\partial P}{\partial \rho e_s}\right|_{\rho,\underline{\boldsymbol{Y}}^\ell,\underline{\boldsymbol{Y}}^v}, \tag{18a}$$

$$\xi_i^\ell = \left.\frac{\partial \rho e_s}{\partial \rho Y_i}\right|_{P,\rho Y_{j\neq i}^\ell,\rho\underline{\boldsymbol{Y}}^v}, \tag{18b}$$

$$\xi_i^v = \left.\frac{\partial \rho e_s}{\partial \rho Y_i}\right|_{P,\rho Y_{j\neq i}^v,\rho\underline{\boldsymbol{Y}}^\ell}. \tag{18c}$$

It can then be shown (cf. Appendix B) that these terms read

$$\zeta = \frac{1}{(\rho c_\mathrm{p})_\mathrm{mix}\frac{\beta_\mathrm{mix}}{\alpha_\mathrm{mix}} - \alpha_\mathrm{mix} T}, \tag{19a}$$

$$\xi_i^\phi = h_{\phi,i} - \frac{(\rho c_\mathrm{p})_\mathrm{mix}}{\alpha_\mathrm{mix}} v_{\phi,i}, \tag{19b}$$

with the *mixture* properties defined for any quantity ψ as

$$\psi_\mathrm{mix} = z_\ell \psi_\ell + (1 - z_\ell)\psi_v. \tag{20}$$

Therefore, the Jacobian matrix of the 4-equation model can be expressed in terms of coefficients that are directly obtained from the equation of state of each phase.

Also, the speed of sound for the 4-equation model is given by

$$c^2 = \left.\frac{\partial P}{\partial \rho}\right|_{s,\underline{\boldsymbol{Y}}^\ell,\underline{\boldsymbol{Y}}^v}. \tag{21}$$

After some derivations provided in Appendix B, this reads

$$c^2 = \frac{\bar{c_\mathrm{p}}}{\rho\beta_\mathrm{mix}\bar{c_\mathrm{p}} - \alpha_\mathrm{mix}^2 T}. \tag{22}$$

2.3.1. Boundary conditions

As for the 3-equation model, the characteristic boundary condition formulation of [42] is used. It is important to note that the source terms relative to the relaxation towards equilibrium must be taken into account when applying the boundary conditions. In this respect, the characteristic boundary conditions formulation is taken identical to the one of the 3-equation model.

2.4. Numerics for diffusion operators and stabilization method

The diffusion operators are discretized following the local stencil "2-Δ" finite-element formulation of [39]. The numerical method is stabilized by applying localized artificial viscosity to guarantee both accuracy and stability, following the technique of [11].

3. Thermodynamic closures

3.1. Cubic equations of state

The Soave-Redlich-Kwong (SRK) and Peng-Robinson (PR) cubic EoS are used [6, 5]. They are given by the following explicit relation between the pressure P, temperature T, density ρ and mixture composition $\underline{\boldsymbol{Y}}$:

$$P(\rho, T, \underline{\boldsymbol{Y}}) = \frac{\rho \bar{r} T}{1 - \bar{b}\rho} - \frac{\bar{a}(T)\rho^2}{1 + \varepsilon_1 \bar{b}\rho - \varepsilon_2 \bar{b}^2 \rho^2} \tag{23}$$

with the mixture covolume $\bar{b}$ and attractive coefficient $\bar{a}$ computed following the van der Waals mixing laws [45]:

$$\bar{a}(T) = \sum_{i=1}^{N_s} Y_i Y_j \left(1 - k_{ij}\right) \sqrt{a_i(T) a_j(T)}, \tag{24a}$$

$$\bar{b} = \sum_{i=1}^{N_s} Y_i b_i, \tag{24b}$$

with k_{ij} the binary interaction coefficients. One has $\bar{r} = \mathcal{R}/\bar{\mathrm{W}}$, where $\bar{\mathrm{W}}$ is the mixture molar mass. The attraction coefficient and covolume of pure components $a_i(T)$ and b_i are given by

$$a_i(T) = \Phi_{c,i} \Psi_i(T)^2, \tag{25a}$$

$$b_i = b_0 \frac{r_i T_{c,i}}{P_{c,i}}, \tag{25b}$$

with

$$\Phi_{c,i} = \Phi_0 \frac{r_i^2 T_{c,i}^2}{P_{c,i}}, \tag{26a}$$

$$\Psi_i(T) = 1 + \left(\psi_0 + \psi_1 \omega_i + \psi_2 \omega_i^2\right) \left(1 - \sqrt{\frac{T}{T_{c,i}}}\right), \tag{26b}$$

$$\tag{26c}$$

the parameters ε_1 and ε_2, Φ_0 and ψ_0, ψ_1, ψ_2 being given in Table 1, and $r_i = \mathcal{R}/W_i$. $P_{c,i}$ and $T_{c,i}$ denote respectively the critical pressure and temperature of component i.

EoS	ε_1	ε_2	ε_{12}	b_0	Φ_0	ψ_0	ψ_1	ψ_2
SRK	0	1	1	0.0866	0.0778	0.4850	1.5517	-0.1561
PR	2	1	$2\sqrt{2}$	0.4275	0.4572	0.3746	1.5422	-0.2699

Table 1: Cubic EoS parameters for SRK and PR. We define $\varepsilon_{12} = \sqrt{\varepsilon_1^2 + 4\varepsilon_2}$.

3.2. Thermodynamic equilibrium for a single-component fluid

The description of the thermodynamics of two-phase mixtures is a cornerstone of diffuse interface models addressing phase change phenomena [46, 27, 31]. The present section describes the methodology for the practical equilibrium computation for cubic EoS closures and provides the differentials terms involved in the Jacobian matrix for the 3-equation model (see Section 2).

3.2.1. Equilibrium formulation

The two-phase equilibrium for single-component mixtures is characterized by the following equality:

$$\begin{cases} P_\ell = P_v, & \text{(27a)} \\ T_\ell = T_v, & \text{(27b)} \\ g_\ell = g_v. & \text{(27c)} \end{cases}$$

Using the *corresponding state principle*, it is possible to reduce the search for the saturated states of any pure component to a unique and universal computation for a given cubic EoS. This is described in Appendix A.

3.2.2. Practical computation

The computation of the thermodynamic state from the transported variables (ρ^n, e_s^n) is now presented. First, a Newton-Raphson method is performed using directly the EoS, to find the temperature T^{m}, assuming a single-phase state.

Then, the stability of the couple (ρ^n, T^{m}) is evaluated, verifying that $\rho^n \notin [\rho_v(T^{\mathrm{m}}), \rho_\ell(T^{\mathrm{m}})]$. If the single-phase state is stable, the temperature T^{m} is kept. If the state is unstable, it is necessary to undergo another Newton-Raphson iterative method, with objective function:

$$F^{\mathrm{NR}}(T) = e_s - \left[y_\ell(\rho^n, T) e_\ell^{\mathrm{sat}}(T) + \left(1 - y_\ell(\rho^n, T)\right) e_v^{\mathrm{sat}}(T) \right], \tag{28}$$

where the liquid mass fraction is given by:

$$y_\ell(\rho, T) = \left(\frac{\rho - \rho_v^{\mathrm{sat}}(T)}{\rho_\ell^{\mathrm{sat}}(T) - \rho_v^{\mathrm{sat}}(T)} \right) \frac{\rho_\ell^{\mathrm{sat}}(T)}{\rho} \tag{29}$$

and the saturation energy of phase $\phi \in \{\ell, v\}$ is $e_\phi^{\mathrm{sat}}(T) = e_s(\rho_\phi^{\mathrm{sat}}(T), T)$.

3.2.3. Differentials of thermodynamic quantities along the two-phase equilibrium

The differentials of the thermodynamic quantities along the two-phase equilibrium, which are necessary for the derivation of the Jacobian matrices (see Section 2), can be obtained by means of the Clausius-Clapeyron relation. Assuming the two-phase thermodynamic equilibrium (27), any variation of the state verifies

$$\mathrm{d}g_\ell = \mathrm{d}g_v. \tag{30}$$

Then, using the identity

$$\mathrm{d}g_\phi = -s_\phi \, \mathrm{d}T_\phi + \frac{1}{\rho_\phi} \, \mathrm{d}P_\phi, \tag{31}$$

and the equality of pressure and temperature differential between phases, one obtains the Clausius-Clapeyron relation:

$$\left.\frac{\mathrm{d}P}{\mathrm{d}T}\right|_{\mathrm{sat}} = \frac{\rho_v \rho_\ell \left(s_v - s_\ell\right)}{\rho_\ell - \rho_v} = \frac{\rho_v \rho_\ell \left(h_v - h_\ell\right)}{T \left(\rho_\ell - \rho_v\right)}. \tag{32}$$

One can introduce *saturation derivatives*: for any thermodynamic quantity ψ_ϕ of phase $\phi \in \{\ell, v\}$ at saturation, one defines

$$\left.\frac{\mathrm{d}\psi_\phi}{\mathrm{d}T}\right|_{\mathrm{sat}} = \frac{\mathrm{d}\psi_\phi(T, P^{\mathrm{sat}}(T))}{\mathrm{d}T} = \left.\frac{\partial \psi_\phi}{\partial T}\right|_P + \left.\frac{\mathrm{d}P}{\mathrm{d}T}\right|_{\mathrm{sat}} \left.\frac{\partial \psi_\phi}{\partial P}\right|_T, \tag{33}$$

and

$$\left.\frac{\mathrm{d}\psi_\phi}{\mathrm{d}P}\right|_{\mathrm{sat}} = \frac{\mathrm{d}\psi_\phi(T^{\mathrm{sat}}(P), P)}{\mathrm{d}P} = \left.\frac{\mathrm{d}T}{\mathrm{d}P}\right|_{\mathrm{sat}} \left.\frac{\partial \psi_\phi}{\partial T}\right|_P + \left.\frac{\partial \psi_\phi}{\partial P}\right|_T. \tag{34}$$

For example, for the density and sensible energy of each phase $\phi \in \{\ell, v\}$, this yields:

$$\left.\frac{\mathrm{d}\rho_\phi}{\mathrm{d}T}\right|_{\mathrm{sat}} = -\rho_\phi\alpha_\phi + \rho_\phi\beta_\phi \left.\frac{\mathrm{d}P}{\mathrm{d}T}\right|_{\mathrm{sat}}. \tag{35}$$

$$\left.\frac{\mathrm{d}e_\phi}{\mathrm{d}T}\right|_{\mathrm{sat}} = \frac{\beta_\phi P - \alpha_\phi T}{\rho_\phi} \left.\frac{\mathrm{d}P}{\mathrm{d}T}\right|_{\mathrm{sat}} + c_{p,\phi} - \frac{\alpha_\phi P}{\rho_\phi}. \tag{36}$$

In order to compute the coefficients ξ and ζ, one writes the differential of the mixture sensible energy (5b):

$$\mathrm{d}(\rho e_s) = z_\ell\,\mathrm{d}(\rho_\ell e_\ell) + (1-z_\ell)\,\mathrm{d}(\rho_v e_v) + (\rho_\ell e_\ell - \rho_v e_v)\,\mathrm{d}z_\ell. \tag{37}$$

Using the differential of the liquid volume fraction at equilibrium:

$$\mathrm{d}z_\ell = -\frac{1}{\rho_\ell - \rho_v}\left[z_\ell \left.\frac{\mathrm{d}\rho_\ell}{\mathrm{d}T}\right|_{\mathrm{sat}} + (1-z_\ell)\left.\frac{\mathrm{d}\rho_v}{\mathrm{d}T}\right|_{\mathrm{sat}}\right]\left.\frac{\mathrm{d}T}{\mathrm{d}P}\right|_{\mathrm{sat}}\mathrm{d}P + \frac{1}{\rho_\ell - \rho_v}\,\mathrm{d}\rho, \tag{38}$$

it comes that

$$\xi = \frac{1}{\rho}\left(\rho h - T\left.\frac{\mathrm{d}T}{\mathrm{d}P}\right|_{\mathrm{sat}}^{-1}\right), \tag{39a}$$

$$\zeta = \left[\left.\frac{\mathrm{d}T}{\mathrm{d}P}\right|_{\mathrm{sat}}(\rho c_{\mathrm{p}})_{\mathrm{mix}} - 2T\alpha_{\mathrm{mix}} + T\left.\frac{\mathrm{d}T}{\mathrm{d}P}\right|_{\mathrm{sat}}^{-1}\beta_{\mathrm{mix}}\right]^{-1}. \tag{39b}$$

The speed of sound can similarly be computed using

$$c^2 = -\left.\frac{\partial s}{\partial P}\right|_\rho^{-1}\left.\frac{\partial s}{\partial \rho}\right|_P, \tag{40}$$

the mixture entropy being given by

$$\rho s = z_\ell\rho_\ell s_l + (1-z_\ell)\rho_v s_v, \tag{41}$$

and the differential of the entropy of phase $\phi \in \{\ell, v\}$:

$$\left.\frac{\mathrm{d}s_\phi}{\mathrm{d}P}\right|_{\mathrm{sat}} = -\frac{\alpha_\phi}{\rho_\phi} + \frac{c_{p,\phi}}{T}\left.\frac{\mathrm{d}T}{\mathrm{d}P}\right|_{\mathrm{sat}}. \tag{42}$$

The speed of sound finally reads

$$c^2 = \left(\rho\left[\frac{1}{\beta_{\mathrm{mix}}}\left(\beta_{\mathrm{mix}} - \alpha_{\mathrm{mix}}\left.\frac{\mathrm{d}T}{\mathrm{d}P}\right|_{\mathrm{sat}}\right)^2 + \frac{(\rho c_{\mathrm{v}})_{\mathrm{mix}}}{T}\left.\frac{\mathrm{d}T}{\mathrm{d}P}\right|_{\mathrm{sat}}^2\right]\right)^{-1}, \tag{43}$$

which is always positive and therefore guarantees the hyperbolicity of the system.

3.3. Exact thermodynamic equilibrium for a multicomponent fluid

3.3.1. Practical computation for the exact equilibrium formulation

For a multicomponent fluid, the two-phase homogeneous equilibrium is characterized by the following conditions:

$$\begin{cases} P_\ell = P_v, & \text{(44a)} \\ T_\ell = T_v, & \text{(44b)} \\ g_{\ell,i} = g_{v,i}, \ \forall i \in [\![1, N_s]\!]\,. & \text{(44c)} \end{cases}$$

The effective computation of the vapour-liquid equilibrium follows the guidelines of [47] as in [31].

From the transported state $(\rho^n \underline{\mathbf{Y}}^n, e_s^n)$, the corresponding single-phase solution $(T^{\mathrm{m}}, P^{\mathrm{m}})$ is computed, using directly the EoS, by means of a Newton solver. Then, the stability of the one-phase state is tested, using the *tangent plane distance* analysis of [47]. If the single-phase state is found stable, then it is the solution. Otherwise, the two-phase equilibrium state corresponding to $(\rho^n \underline{\mathbf{Y}}^n, e_s^n)$ must be evaluated. This is achieved by means of two nested loops. The outer loop consists in a Newton solver that iterates over the temperature $T^{(k)}$ and pressure $P^{(k)}$ to cancel the objective function f:

$$f\left(\begin{bmatrix} T \\ P \end{bmatrix}\right) = \begin{bmatrix} \rho^n - \rho^{\mathrm{eq}}(T, P, \underline{\mathbf{Y}}^n) \\ e_s^n - e_s^{\mathrm{eq}}(T, P, \underline{\mathbf{Y}}^n) \end{bmatrix}, \tag{45}$$

the Jacobian matrix of which being computed numerically. The equilibrium state $[\rho^{\mathrm{eq}}, e_s^{\mathrm{eq}}]\,(T, P, \underline{\mathbf{Y}}^n)$ is obtained by means of an inner loop which consists in the successive substitution method of [47].

In the context of the exact multicomponent equilibrium, to the authors knowledge, there exist no explicit analytical formula to describe the variations of the thermodynamic variables along the equilibrium. In this respect, the use of the 3-equation model requires to compute numerically the Jacobian matrix of the flux function. This implies a high computational cost, as it involves multiple equilibrium computations. For this reason, the use of the 4-equation model is preferred with the exact formulation of the two-phase equilibrium.

Because the boundary conditions for the 4-equation model with stiff relaxation to equilibrium must be computed identically to the 3-equation model in order to account for the relaxation source term, numerical differentiation has to be used at the boundary points to obtain the proper characteristic boundary condition formulation, when applying the 4-equation model with relaxation.

This strategy is similar to the one used by [30, 31, 32]. It is computationally expensive, as it requires to search for the global minimum of a function of N_s variables to evaluate the stability of the single-phase mixture, and then requires an additional iterative method within a N_s-dimension space to find the stable multiphase state. In this respect, the exact multiphase equilibrium computation for multicomponent flows, especially when going towards detailed chemical mechanisms for combustion, may become computationally out of range. Also, it may sometimes converge with difficulty, as mentioned by [31].

This motivated the formulation of the simplified equilibrium approximation described in Section 3.4.

3.4. Approximate two-phase equilibrium for a multicomponent fluid

3.4.1. Equilibrium formulation

In the present context of diffuse interface models, the interface region where the two-phase states may be encountered consists in an artificial mixture zone. In this respect, an approximate equilibrium formulation is then proposed, that guarantees the hyperbolicity of the system while keeping an identical algorithm complexity for any number of components, to describe this artificial mixture.

The approximate equilibrium consists in assuming that both phases have equal composition. In other words, for any species i, its mass fraction within the liquid phase $Y_{i,\ell} = \frac{m_i^\ell}{m_\ell}$ and within the vapour phase $Y_{i,v} = \frac{m_i^v}{m_v}$ are assumed to be equal $Y_{i,\ell} = Y_{i,v}$. Then, they are equal to the overall species mass fraction, and the approximated equilibrium can be summarized by the following assumption:

$$Y_i = Y_{i,\ell} = Y_{i,v}. \tag{46}$$

Under this assumption, the equilibrium condition reads as for the single-component case:

$$\begin{cases} P_\ell = P_v, & \text{(47a)} \\ T_\ell = T_v, & \text{(47b)} \\ g_\ell = g_v, & \text{(47c)} \end{cases}$$

and the practical computation can also be achieved using the tabulation explained in Section 3.2.

3.4.2. Differentials of thermodynamic quantities along the two-phase equilibrium

Under the approximate equilibrium assumption, for any variation of the thermodynamic state, the Gibbs energy of the liquid phase and of the vapour phase remain equal, so that equation (30) is verified. In this respect an *extended* Clausius-Clapeyron relation can be derived, which writes:

$$\mathrm{d}P^{\mathrm{sat}} = \frac{\rho_\ell \rho_v \left(h_v - h_\ell\right)}{T(\rho_\ell - \rho_v)} \mathrm{d}T + \frac{\rho_\ell \rho_v}{\rho_\ell - \rho_v} \sum_{i=1}^{N_s} \left(g_{v,i} - g_{\ell,i}\right) \mathrm{d}Y_i. \tag{48}$$

Then, the differentials of the saturation density and energy of phase $\phi \in \{\ell, v\}$ can be written:

$$\begin{aligned} \mathrm{d}\rho_\phi = &\left(\rho_\phi \beta_\phi - \rho_\phi \alpha_\phi \left.\frac{\partial T}{\partial P}\right|_{\mathrm{sat},\underline{\boldsymbol{Y}}} \right) \mathrm{d}P \\ &+ \frac{\rho_\phi}{\rho} \sum_{i=1}^{N_s} \left[\alpha_\phi \left.\frac{\partial T}{\partial P}\right|_{\mathrm{sat},P,Y_{j\neq i}} - \rho_\phi v_{\phi,i} \right] \mathrm{d}(\rho Y_i), \end{aligned} \tag{49a}$$

$$\begin{aligned} \mathrm{d}e_\phi = &\left[\left(c_{p,\phi} - \frac{\alpha_\phi P}{\rho_\phi} \right) \left.\frac{\partial T}{\partial P}\right|_{\mathrm{sat},\underline{\boldsymbol{Y}}} + \frac{\beta_\phi P - \alpha_\phi T}{\rho_\phi} \right] \mathrm{d}P \\ &+ \frac{1}{\rho} \sum_{i=1}^{N_s} \left[e_{\phi,i} - \left(c_{p,\phi} - \frac{\alpha_\phi P}{\rho_\phi} \right) \left.\frac{\partial T}{\partial P}\right|_{\mathrm{sat},P,Y_{j\neq i}} \right] \mathrm{d}(\rho Y_i), \end{aligned} \tag{49b}$$

and the liquid volume fraction differential is:

$$\begin{aligned} \mathrm{d}z_\ell = &- \frac{1}{\rho_\ell - \rho_v} \left[z_\ell \left.\frac{\mathrm{d}\rho_\ell}{\mathrm{d}P}\right|_{\mathrm{sat}} + (1 - z_\ell) \left.\frac{\mathrm{d}\rho_v}{\mathrm{d}P}\right|_{\mathrm{sat}} \right] \mathrm{d}P \\ &+ \sum_{i=1}^{N_s} \frac{1}{\rho_\ell - \rho_v} \left[1 - z_\ell \left.\frac{\mathrm{d}\rho_\ell}{\mathrm{d}Y_i}\right|_{\mathrm{sat},P,Y_{j\neq i}} - (1 - z_\ell) \left.\frac{\mathrm{d}\rho_v}{\mathrm{d}Y_i}\right|_{\mathrm{sat},P,Y_{j\neq i}} \right] \mathrm{d}(\rho Y_i). \end{aligned} \tag{50}$$

The Jacobian coefficients then read:

$$\xi_i = \frac{1}{\rho}\left[\left((\rho c_{\mathrm{p}})_{\mathrm{mix}} - T\,\frac{\partial T^{\mathrm{sat}}}{\partial P}\bigg|_{\underline{\boldsymbol{Y}}}^{-1}\alpha_{\mathrm{mix}}\right)\frac{\partial T^{\mathrm{sat}}}{\partial Y_i}\bigg|_{Y_{j\neq i}} + (\rho h_i)_{\mathrm{mix}} - T\,\frac{\partial T^{\mathrm{sat}}}{\partial P}\bigg|_{\underline{\boldsymbol{Y}}}^{-1}(\rho v_i)_{\mathrm{mix}}\right], \tag{51}$$

$$\zeta = \left[\frac{\partial T^{\mathrm{sat}}}{\partial P}\bigg|_{\underline{\boldsymbol{Y}}} C_{p,\mathrm{mix}} - 2T\alpha_{\mathrm{mix}} + T\,\frac{\partial T^{\mathrm{sat}}}{\partial P}\bigg|_{\underline{\boldsymbol{Y}}}^{-1}\beta_{\mathrm{mix}}\right]^{-1}. \tag{52}$$

For the approximate equilibrium formulation, the speed of sound of the 3-equation model has the same expression as the single-component case (43), since this quantity is defined considering fixed mixture composition.

3.5. Comparisons between the exact and approximate equilibriums

We now consider a H_2-O_2 interface, for which we compute both the exact and approximate equilibriums. The pressure is set to $P = 10$ bar, as this will be the operating pressure for the simulations of Section 6, and to $P = 20$ bar. The input profiles for the density and species are given as:

$$\begin{cases} \rho Y_{\mathrm{H_2}}(x) = \rho^0_{\mathrm{H_2}}\left[1 - f_\rho(x)\right], & \text{(53a)} \\ \rho Y_{\mathrm{O_2}}(x) = \rho^0_{\mathrm{O_2}} f_\rho(x), & \text{(53b)} \end{cases}$$

with the values $\rho^0_{\mathrm{H_2}} = 0.8$ kg/m^3 and $\rho^0_{\mathrm{O_2}} = 1200$ kg/m^3. The profile f_ρ is given by:

$$f_\rho(x) = \frac{1}{2}\left[1 + \mathrm{erf}\left(10\left(x - 1/2\right)\right)\right], \tag{54}$$

where erf is the *error function*, defined as

$$\mathrm{erf}(x) = \frac{1}{\sqrt{\pi}}\int_{-x}^{x} e^{-\tau^2}\,\mathrm{d}\tau. \tag{55}$$

The results of the equilibrium computations are presented in figure 1.

The obtained profiles are very similar. The approximate equilibrium tends to slightly shift the profiles towards the cold/pure-O_2 region. The temperature values obtained within the interface are close, and the widths of the two-phase diffuse interface region, where $y_\ell \in]0, 1[$ are almost equal.

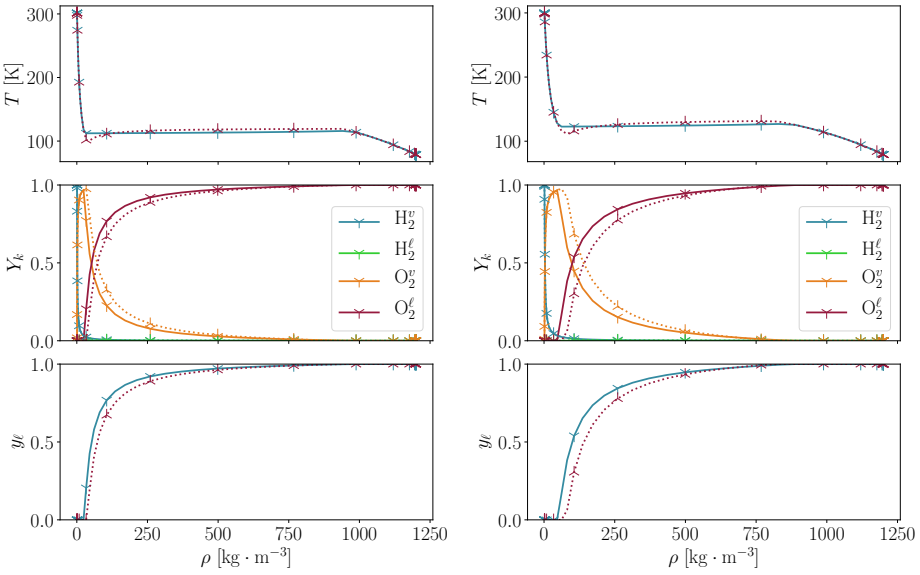

(a) 10 bar

(b) 20 bar

Figure 1: Comparison of the thermodynamic quantities within an interface at $P = 10$ bar and $P = 20$ bar for the exact and approximate equilibriums, considering an H_2-O_2 mixture. Solid lines denote the profiles for the exact equilibrium computation. Dotted lines represent the approximate equilibrium computations.

Note that when going to higher pressures, typically above the critical pressure of the pure components (see figure 2), the approximate computation appears not to retrieve a two-phase region, the liquid volume fraction switching directly from zero to one without intermediary values. This can be explained by the fact that the approximate equilibrium formulation, being similar to a single-component computation, addresses mechanical instabilities but not chemical instabilities. As the mechanical instabilities vanish when the pressure is too high compared to the critical pressure of the pure components, the approximate equilibrium formulation does not allow to retrieve the unstable zone. Therefore, computations in pressure ranges above the pure components critical pressures require the exact multicomponent equilibrium computation.

Note that at even higher pressures (see figure 3), there is no more instability,

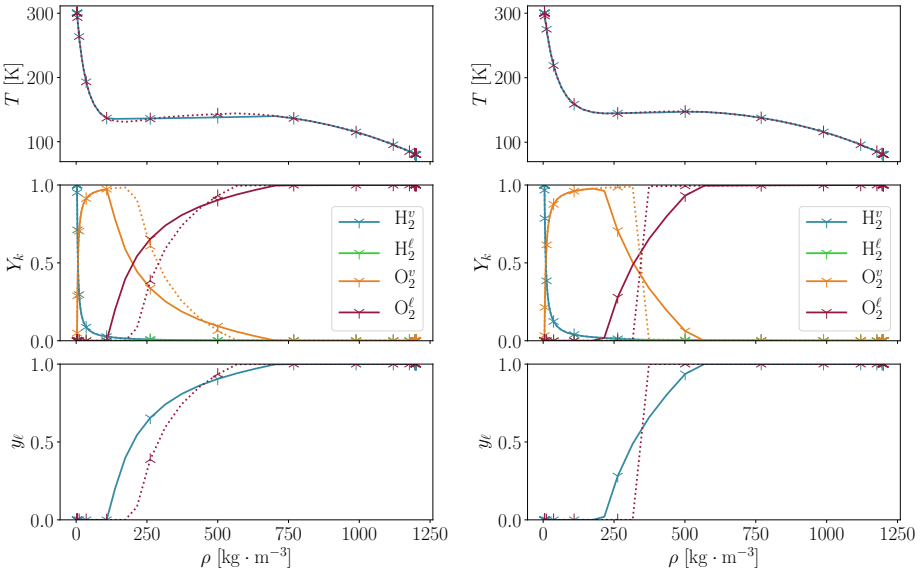

(a) 40 bar (b) 60 bar

Figure 2: Comparison of the thermodynamic quantities within an interface at $P = 40$ bar and $P = 60$ bar for the exact and approximate equilibriums, considering an H_2-O_2 mixture. Solid lines denote the profiles for the exact equilibrium computation. Dotted lines represent the approximate equilibrium computations. The approximate computation at 60 bar displays no thermodynamic instability, switching from pure "vapour-like" fluid with $y_\ell = 0$ to pure "liquid-like" fluid with $y_\ell = 1$.

even for the exact formulation, so that both computations predict the same thermodynamic state.

To summarize, the approximation introduced provides a computationally efficient way to guarantee the hyperbolic character of the model and to handle the presence of a liquid-gas interface in the subcritical domain. This is done at the cost of approximate values for the temperature and liquid volume fraction for subcritical states, within the interface region, and its use is restricted to low-pressure states as it does not allow to predict phase separation due to chemical instabilities. In the scope of the present article, dedicated to the integration of multifluid methods into a Taylor-Galerkin framework, it however allows to

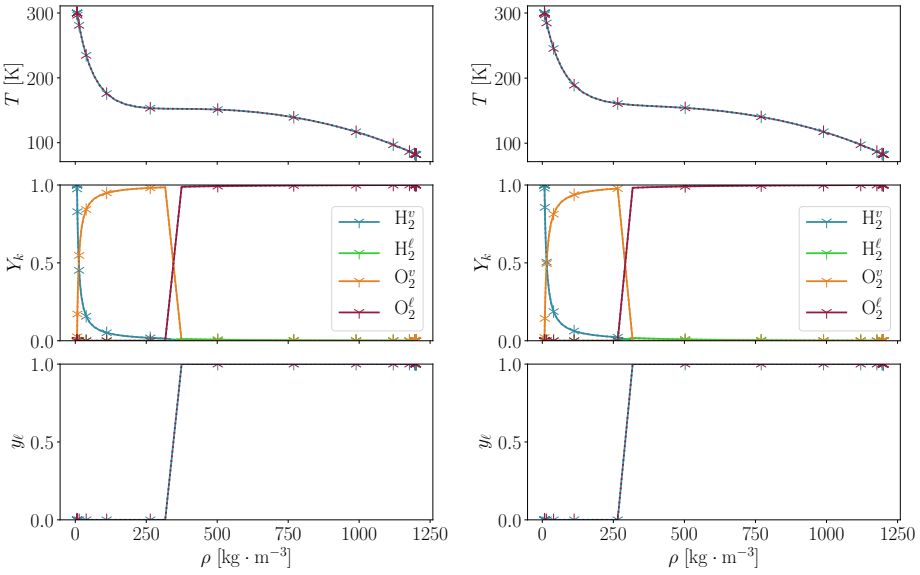

(a) 80 bar (b) 100 bar

Figure 3: Comparison of the thermodynamic quantities within an interface at $P = 80$ bar and $P = 100$ bar for the exact and approximate equilibriums, considering an H_2-O_2 mixture. Solid lines denote the profiles for the exact equilibrium computation. Dotted lines represent the approximate equilibrium computations.

provide a thermodynamic closure that analytically closes the 3-equation model for the proper validation of the developments and implementation.

4. One-dimensional validations

In order to validate the derivations, implementation and behaviour of the 3-equation and 4-equation models, one-dimensional simulations are performed. This section focuses on the evaluation and validation of the transport strategy, so that the LES and combustion models are not considered. The thermodynamic closure used is the approximate multicomponent equilibrium formulation of section 3.4. Numerical stabilization is only applied on test case of section 4.3, otherwise no diffusion (whether physical or artificial) is considered in the tests.

4.1. Acoustic perturbations transport and boundary conditions

The first test case consists in validating the transport and reflection of acoustic perturbations using fully reflecting characteristic boundary conditions. The initial state consists in a homogeneous O_2-N_2 mixture state with velocity $u_0 = 0$ m/s, pressure $P_0 = 1$ MPa and density $\rho_0 = 100$ kg/m^3 with composition $Y^0_{O_2} = 1 - Y^0_{N_2} = 0.8$, over which Gaussian forward and backward acoustic perturbations are superimposed. The left boundary condition is an inlet with imposed density ρ_0, composition $\underline{\boldsymbol{Y}}^0$ and velocity u_0, while the right one is an outlet with imposed pressure P_0. The TTGC scheme is applied here, with CFL number 0.9. Snapshots of the simulation are given in Figure 4.

The expected behaviour is observed, as the waves conserve their amplitude after being reflected. Both simulations yield very similar results, as the splitting error introduced by the 4-equation model with relaxation seems to be negligible.

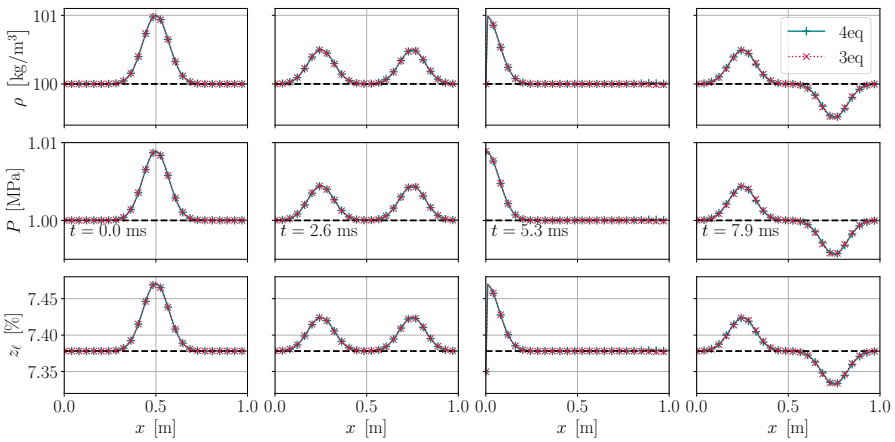

Figure 4: Initially superimposed backward and forward acoustic waves with fully reflecting boundary conditions, for the approximate multicomponent equilibrium computations (3- and 4-equation models). Density and pressure snapshots of the solution. From left to right: initial profile, solution before, during and after interaction with domain boundaries.

4.2. Entropy perturbation and boundary conditions: interface transport

This second test case consists in assessing the ability of the method to transport and evacuate an entropy perturbation. The initial condition consists of a near-pure vapour N_2 bubble in a near-pure liquid O_2 environment, in a unit-length domain with a 100-node mesh. The initial velocity is $u_0 = 10$ m/s and the initial pressure is $P_0 = 1$ MPa. Initial species and density profiles are given by:

$$\rho_0(x) = \left[\frac{1}{\rho_{\min}} + \left(\frac{1}{\rho_{\max}} - \frac{1}{\rho_{\min}} \right) \phi(x) \right]^{-1}, \tag{56a}$$

$$Y_{\mathrm{N_2},0}(x) = Y_{\mathrm{N_2},\min} + (Y_{\mathrm{N_2},\max} - Y_{\mathrm{N_2},\min})\phi(x), \tag{56b}$$

$$Y_{\mathrm{O_2},0}(x) = 1 - Y_{\mathrm{N_2},0}, \tag{56c}$$

with

$$\phi_0(x) = \frac{1}{2} \left[1 + \mathrm{erf} \left(\frac{\sqrt{6}\,(x - 0.1)}{n_{\mathrm{grad}} \Delta x} \right) \right]. \tag{57}$$

Both left and right boundary conditions are characteristic non-reflecting conditions. The TTG4A scheme is applied here, with CFL number 0.9. Snapshots of the simulation are given in Figure 5. For the sake of readability, only the results from the 3-equation model are displayed as the results for the 4-equation model are very similar.

4.3. Advection of a stiff H_2/O_2 interface

As the TTG schemes are centered low-dissipation schemes, their use requires stabilization techniques when advection-dominated problems with strong gradients are simulated. To illustrate the behaviour of the model with such a stabilization technique, a test case consisting in the transport of a H_2-O_2 interface is conducted, similarly to [11]. The initial solution is the following:

$$\rho_0(x) = \left[\frac{1}{\rho_{\min}} + \left(\frac{1}{\rho_{\max}} - \frac{1}{\rho_{\min}} \right) \phi_0(x) \right]^{-1}, \tag{58a}$$

$$Y_{\mathrm{H_2},0}(x) = Y_{\mathrm{H_2},\min} + (Y_{\mathrm{H_2},\max} - Y_{\mathrm{H_2},\min})\phi_0(x), \tag{58b}$$

$$Y_{\mathrm{O_2},0}(x) = 1 - Y_{\mathrm{H_2},0}, \tag{58c}$$

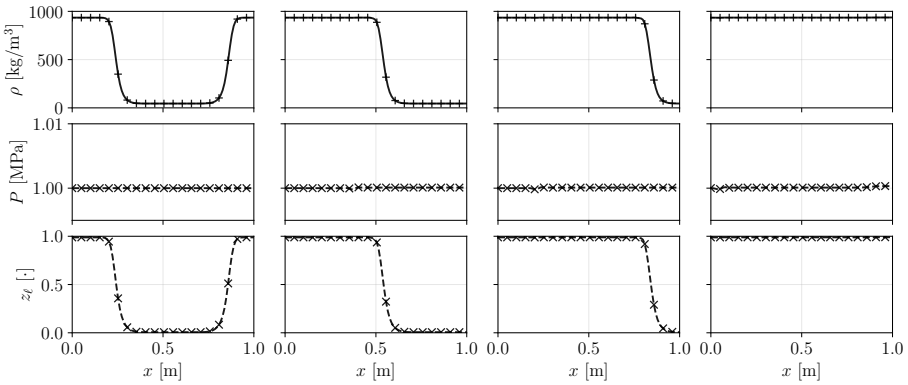

Figure 5: N_2 bubble in O_2 environment transport and evacuation through the boundaries. Snapshots are taken every 300 ms. For the sake of readability, only 1 point out of 5 is marked. Only a slight pressure fluctuation of less than 0.05% of the initial pressure is observed as the interface crosses the boundary.

with $\phi_0(x)$ defined by equation (57). The number of points within the gradient region is set to $n_{\text{grad}} = 4$.

The velocity is constant and equal to 10 m/s and the following values are used: $\rho_{\min} = 13$ kg/m^3, $\rho_{\max} = 980$ kg/m^3 and $Y_{\text{H}_2,\min} = 0$, $Y_{\text{H}_2,\max} = 1$. In this test case, the TTG4A scheme is applied.

The initial pressure field is constant and equal to P_0. Two simulations are run with $P_0 = 1$ MPa, below the critical pressure of H_2, O_2: one using the 3-equation and the other using the 4-equation models. In this configuration, the left-hand side corresponds to pure liquid and the right-hand side to pure vapour. Finally, a reference simulation is run with $P_0 = 8$ MPa, above the critical pressure of H_2, O_2, so that only one supercritical fluid phase is present. A fixed time step $\Delta t = 10^{-3}$ ms is taken for the different simulations.

The results are displayed in Figure 6, which focuses on the zone of interest $x \in [0, 0.3]$ m. The three computations appear to provide a very similar behaviour for the density field. Slight spurious oscillations due to the dispersive nature of the high-order scheme used are observed. Note that in the absence of localized artificial diffusion, these oscillations are stronger and lead to negative density values, resulting in a simulation crash.

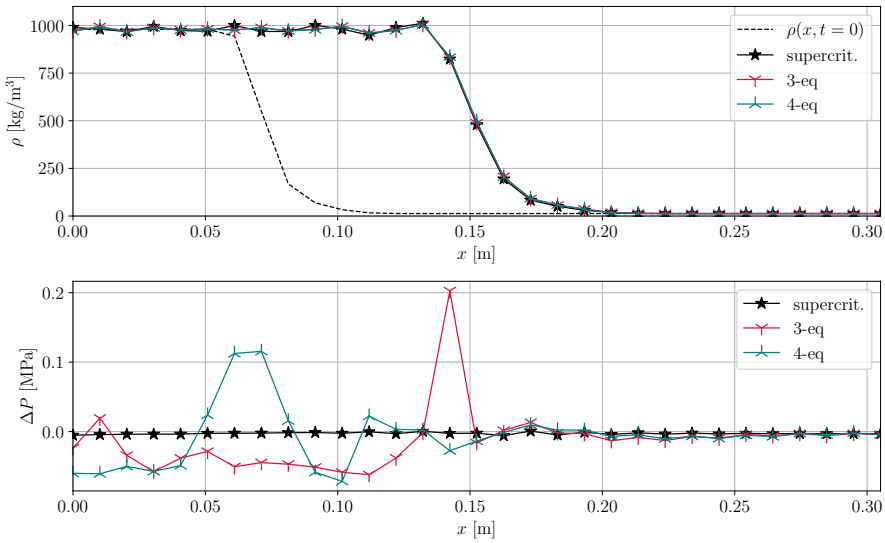

Figure 6: Transport of an H_2-O_2 interface: density field and pressure-error $\Delta P = P - P_0$ field, after a time $t = 8$ ms, for the supercritical case and the subcritical 3-equation and 4-equation cases.

Regarding the pressure field, one observes spurious noise for the 3-equation and 4-equation cases. This noise appears to be generated intermittently at the point where the fluid state switches from pure liquid to the two-phase mixture interface region and is then evacuated through the liquid phase, as depicted by Figure 6. This behaviour may be due to the sound speed jump across the limit between pure phase and two-phase mixture that is inherent to the homogeneous equilibrium assumptions [48]. Despite the relatively high intensity of the oscillations, the density transport appears not to be harmed (see Figure 6), compared to the supercritical computation. This is attributed to the high spatial frequency of these oscillations and the weakly compressible nature of the liquid O_2 phase. Note that the same observations can be made in the 3D case (see Section 6).

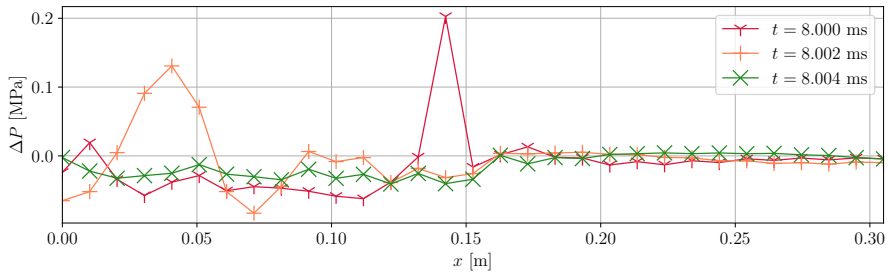

Figure 7: Transport of an H_2-O_2 interface with the 3-equation model: successive snapshots showing noise generation at the liquid–two-phase interface and its evacuation. The noise observed with the 4-equation model are similar and is not displayed for the sake of readability.

4.4. Convergence order validation

4.4.1. Convergence order within the two-phase interface states

This test case consists in verifying the convergence order of the scheme for a smooth test case. For this, a unit-length periodic domain $\Omega = [0, 1]$ m is used, filled with a H_2-O_2 mixture. The initial solution has constant pressure and velocity fields, respectively $P = 1$ MPa and $u_0 = 20$ m/s. The density and species fields are initialized as

$$\rho_0(x) = \rho_{\min} + (\rho_{\max} - \rho_{\min}) f(x), \tag{59a}$$

$$Y_{H_2,0}(x) = Y_{H_2,\min} + (Y_{H_2,\max} - Y_{H_2,\min}) f(x), \tag{59b}$$

$$Y_{O_2,0}(x) = 1 - Y_{H_2,0}, \tag{59c}$$

with the smooth profile function defined as

$$f(x) = \begin{cases} \cos\left(\dfrac{\pi(x - 1/2)}{w}\right)^8 & \text{if } x \in \left[\dfrac{1-w}{2}, \dfrac{1+w}{2}\right], \\ 0 & \text{otherwise,} \end{cases} \tag{60}$$

with width $w = 0.6$ m and the following values: $\rho_{\min} = 100$ kg/m^3, $\rho_{\max} = 500$ kg/m^3 and $Y_{H_2,\min} = 0.4$, $Y_{H_2,\max} = 0.6$.

The TTGC scheme is applied with CFL number 0.9. The mesh is refined successively with $n_x \in \{20, 40, 80, 160, 320\}$. The results obtained are displayed in figure 8.

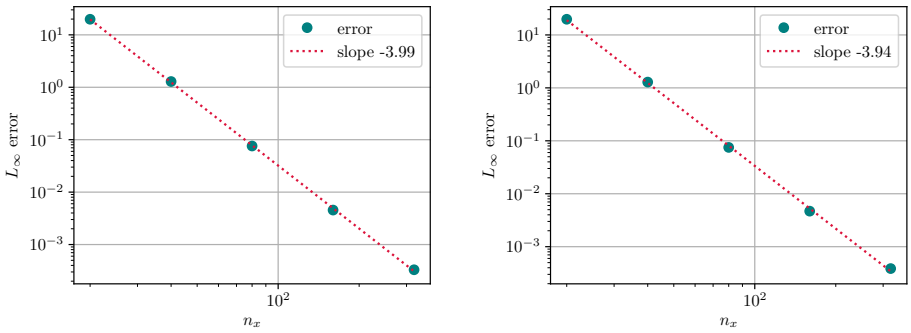

Figure 8: Convergence order of TTGC scheme, for the 3-equation (left) and 4-equation (right) models. The L_∞-norm is computed for the ρ profile after 1 rotation within the periodic domain ($t = 50$ ms)

The high-order convergence rate obtained corresponds properly to the TTGC scheme and superconvergence is even observed, close to 4^{th}-order instead of the theoretically expected 3^{rd}-order [49]. This is attributed to this specific case with a highly smooth function on equally spaced grid and is not to be considered a general property of the implemented method, which is 3^{rd}-order.

4.4.2. Convergence order for the transport of an interface between pure liquid and pure gas phases

In this last case, the transport of an interface separating pure liquid and pure gas phases is considered. The initial condition is periodic, involving two liquid-O_2 – gaseous-N_2 interfaces with the following profiles:

$$\rho_0(x) = \rho_{\min} + (\rho_{\max} - \rho_{\min}) f_{\text{int}}(x), \tag{61a}$$

$$Y_{N_2,0}(x) = Y_{N_2,\min} + (Y_{N_2,\max} - Y_{N_2,\min}) f_{\text{int}}(x), \tag{61b}$$

$$Y_{O_2,0}(x) = 1 - Y_{N_2,0}, \tag{61c}$$

with

$$f_{\text{int}}(x) = \frac{1}{2}\left(1 - \text{erf}\left(\sqrt{6}\frac{(x - x_{\text{int}})}{0.12}\right) + 1 - \text{erf}\left(\sqrt{6}\frac{(1 - x_{\text{int}} - x)}{0.12}\right)\right) \tag{62}$$

and considering $\rho_{\min} = 50$ kg/m^3, $\rho_{\max} = 800$ kg/m^3, $Y_{O_2,\min} = 0$, $Y_{O_2,\max} = 1$, $Y_{N_2,\min} = 0$ and $Y_{N_2,\max} = 1$. This test case corresponds to a N_2 bubble within

a liquid O_2 environment.

The pressure is initially constant and equal to 30 bar. The TTG4A scheme is applied with a CFL of 0.6.

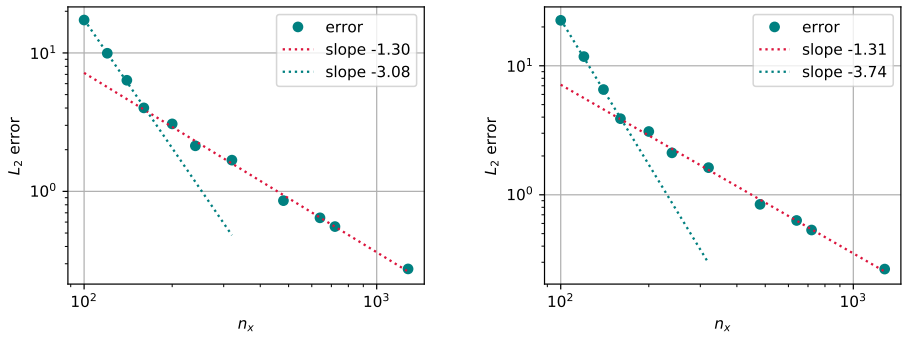

Figure 9: Convergence order of TTG4A scheme, for the 3-equation (left) and 4-equation (right) models. The L_2-norm is computed for the ρ profile after 1 rotation within the periodic domain ($t = 50$ ms)

Figure 9 shows that a strong reduction of the convergence order is observed when transporting an entire interface. The error is also much larger than for the previous case for fine grids. This is attributed to the spurious pressure noise occurring a the interface region's edges, associated with the 3-equation model and the 4-equation model with stiff relaxation to equilibrium. Despite this accuracy deterioration near the interface edges, the numerical strategy remains third-order in the pure phase regions, so that the turbulence and flow properties in the pure phases can still be satisfyingly captured and transported. Furthermore, two regimes of convergence can be identified, with a high-order behaviour at lower resolutions and lower-order at higher resolutions. In this regard, it is interesting to mention that the high-order behaviour is observed until a resolution of up to 30 points in the interface, which is much higher than the typical interface resolution for a realistic computation (cf. section 6).

5. Governing equations for large-eddy simulation

To properly handle the highly turbulent flows considered in this section and in realistic applications, the Large-Eddy Simulation (LES) approach is chosen here. This strategy consists in spatially filtering the conservation equations to remove the small scale turbulent structures that cannot be resolved on affordable grids. The effects of these small structures is then accounted for by means of *sub-grid scale* (SGS) models. Classical gaseous SGS closures are used here, even though it is expected that additional sub-grid scale contributions may have to be considered for two-phase flows. This last point is out of the scope of the present work.

Additional simplifying assumptions are considered. First, surface tension is neglected, which seems reasonable given the very high Weber numbers encountered in the targeted applications. Second, atomisation is neglected so that no droplets are considered at the SGS level. This is a strong hypothesis, as the droplets might influence the flame structure, which will need further development to properly couple the liquid / gas interfaces and a dedicated method for the dispersed phase (see for example [50]).

5.1. The 3-equation model for the LES of reacting flows

The 3-equation models being similar to Euler equations used in gaseous and supercritical flows, similar closure are used here. Thus, the models are those used for the simulation of supercritical reacting flows [11]. This is an assumption that needs further investigations or validations against experimental data of realistic cases.

Governing equations. The Favre-filtered, fully compressible Navier-Stokes equations for the 3-equation model are given by [51]:

$$\frac{\partial \overline{\rho}\widetilde{Y_k}}{\partial t} + \frac{\partial \overline{\rho}\widetilde{Y_k}\widetilde{u}_j}{\partial x_j} = -\frac{\partial \overline{J_{k,j}}}{\partial x_j} - \frac{\partial J^t_{k,j}}{\partial x_j} + \overline{\dot{\omega}_k} \tag{63}$$

$$\frac{\partial \overline{\rho}\widetilde{u}_i}{\partial t} + \frac{\partial \overline{\rho}\widetilde{u}_i\widetilde{u}_j}{\partial x_j} = -\frac{\partial \overline{p}}{\partial x_i} + \frac{\partial \overline{\tau_{i,j}}}{\partial x_j} + \frac{\partial \tau^t_{i,j}}{\partial x_j} \tag{64}$$

$$\frac{\partial \overline{\rho}\widetilde{E}}{\partial t} + \frac{\partial \overline{\rho}\widetilde{u}_j\widetilde{E}}{\partial x_j} = -\frac{\partial \overline{p}\widetilde{u}_j}{\partial x_j} + \frac{\partial \widetilde{u}_i\overline{\tau_{i,j}}}{\partial x_j} - \frac{\partial \overline{q_j}}{\partial x_j} - \frac{\partial q^t_j}{\partial x_j} + \overline{\dot{\omega}_T} \tag{65}$$

where $\overline{\phi}$ and $\tilde{\phi}$ denote spatial and mass-weighted (Favre) spatially filtered quantities. P is the pressure, T the temperature, ρ the density, Y_k is the mass fraction of the species k, u_i represents the velocity vector components, x_i the spatial coordinates, t is the time, E the total sensible energy, $\tau^t_{i,j}$ the sub-grid scale (SGS) stress tensor, q^t_j the SGS energy fluxes, $J^t_{k,j}$ the SGS species fluxes, $\dot{\omega}_k$ the species reaction rate and $\dot{\omega}_T$ the heat release rate. The fluid viscosity and the heat diffusion coefficient are calculated following the Chung *et al.* method [52] and mass diffusion coefficients are deduced from heat diffusivity by assuming a unity Lewis number (Le=1). The Soret and Dufour effects are neglected. The heat flux $\vec{q}$ uses a classical gradient approach. The laminar species flux $\vec{J_k}$ should account for non-ideal molecular effects [53], in order to guarantee positive entropy production from laminar diffusion. Nonetheless, considering the very slight impact of laminar diffusion in the highly turbulent flows envisaged here, the simple Fick's law is used instead [54].

Models. The sub-grid scale (SGS) energy and species fluxes are modeled using the gradient transport assumption, introducing SGS turbulent viscosity ν_t, turbulent species diffusion D_t and turbulent thermal conductivity coefficients

λ^t:

$$\tau_{ij}^t = 2\,\overline{\rho}\,\nu_t\left(\widetilde{S}_{ij} - \frac{1}{3}\delta_{ij}\widetilde{S}_{ll}\right) \quad \text{with} \quad \widetilde{S}_{ij} = \frac{1}{2}\left(\frac{\partial \widetilde{u}_j}{\partial x_i} + \frac{\partial \widetilde{u}_i}{\partial x_j}\right) - \frac{1}{3}\,\frac{\partial \widetilde{u}_k}{\partial x_k}\,\delta_{ij} \tag{66}$$

$$J_{i,k}^t = -\,\overline{\rho}\left(D_t \frac{\partial \widetilde{Y}_k}{\partial x_i}\right) \tag{67}$$

$$q_i^t = -\,\lambda_t \frac{\partial \widetilde{T}}{\partial x_i} + \sum_{k=1}^{N} J_{i,k}^t\,\widetilde{h}_{s,k} \tag{68}$$

with:

$$D_t = \frac{\nu^t}{\mathrm{Sc}_t} \quad \text{and} \quad \lambda_t = \frac{\rho \nu_t c_\mathrm{p}}{\mathrm{Pr}_t} \tag{69}$$

where $h_{s,k}$ is the partial-mass sensible enthalpy of species k, and turbulent Prandtl Pr_t and Schmidt Sc_t numbers are both set to 0.7. In three dimensions, the SGS turbulent viscosity ν_t is modeled with the *wall-adapting large eddy* (WALE) model [55], well-suited for shear flows [56]. ~~In two dimensions, the *dynamic* Smagorinsky model [57] is used.~~

Combustion model. In the present work, combustion is modeled assuming infinitely fast reactions and pure diffusion regime operation. This choice is made correspondingly to typical supercritical diffusion flame simulations [11]. Other combustion models may be investigated, but this is out of the scope of the present article. Species equilibrium is assumed in this work. All the species are then deduced from equilibrium calculations as a function of the mixture fraction Z. In order to properly represent the temperature over the whole mixture fraction domain for the H_2-O_2 case considered in this calculation, four species (H_2O, H_2, O_2 and OH) are considered here for cases involving hydrogen - oxygen combustion. Filtered mass fractions are computed using a β-pdf [51, 58]:

$$\widetilde{Y_k}(\widetilde{Z}, \widetilde{Z''^2}) = \int_0^1 Y_k(Z^*) P(Z^*, x, t)\,\mathrm{d}Z^* \tag{70}$$

where P is the β-pdf depending on $\widetilde{Z}$ and $\widetilde{Z''^2}$, the filtered variance of the mixture fraction. Both $\widetilde{Z}$ and $\widetilde{Z''^2}$ are transported in the simulation [59]:

$$\frac{\partial \overline{\rho}\widetilde{Z}}{\partial t} + \nabla \cdot (\overline{\rho}\widetilde{Z}\widetilde{u}) = \nabla \cdot (\overline{\rho}(D + D_t)\nabla \widetilde{Z}) \tag{71}$$

$$\frac{\partial \overline{\rho}\widetilde{Z''^2}}{\partial t} + \nabla \cdot (\overline{\rho}\widetilde{Z''^2}\widetilde{u}) = \nabla \cdot (\overline{\rho}(D + D_t)\nabla \widetilde{Z''^2}) + 2\overline{\rho}D_t \|\nabla \widetilde{Z}\|^2 - 2\overline{\rho}D_t \frac{\widetilde{Z''^2}}{{\Delta_x}^2} \tag{72}$$

Finally the filtered reaction rate $\overline{\dot{\omega}_k}$ is determined from a relaxation between the tabulated filtered mass fraction $\widetilde{Y_k}(\widetilde{Z}, \widetilde{Z''^2})$ and the one transported assuming pure mixing $\widetilde{Y_k^+}$ [60, 61]:

$$\overline{\dot{\omega}_k} = \overline{\rho}\frac{\widetilde{Y_k}(\widetilde{Z}, \widetilde{Z''^2}) - \widetilde{Y_k^+}}{\Delta t} \tag{73}$$

where Δt is the time step. The filtered heat release rate is then computed from $\overline{\dot{\omega}_k}$:

$$\overline{\dot{\omega}_T} = -\sum_{k=1}^{N_s} \Delta h^0_{f,k} \overline{\dot{\omega}_k} \tag{74}$$

where $\Delta h^0_{f,k}$ is the formation enthalpy of species k.

5.2. The 4-equation model for the LES of reacting flows

Governing equations. The Favre-filtered, fully compressible Navier-Stokes equations for the 4-equation model are given by:

$$\frac{\partial \overline{\rho}\widetilde{Y}_k^\phi}{\partial t} + \frac{\partial \overline{\rho}\widetilde{Y}_k^\phi \widetilde{u}_j}{\partial x_j} = -\frac{\partial \overline{J^\phi_{k,j}}}{\partial x_j} - \frac{\partial J^{t,\phi}_{k,j}}{\partial x_j} + \overline{\dot{\omega}_k^\phi} \tag{75a}$$

$$\frac{\partial \overline{\rho}\widetilde{u}_i}{\partial t} + \frac{\partial \overline{\rho}\widetilde{u}_i\widetilde{u}_j}{\partial x_j} = -\frac{\partial \overline{p}}{\partial x_i} + \frac{\partial \overline{\tau_{i,j}}}{\partial x_j} + \frac{\partial \tau^t_{i,j}}{\partial x_j} \tag{75b}$$

$$\frac{\partial \overline{\rho}\widetilde{E}}{\partial t} + \frac{\partial \overline{\rho}\widetilde{u}_j\widetilde{E}}{\partial x_j} = -\frac{\partial \overline{p}\widetilde{u}_j}{\partial x_j} + \frac{\partial \widetilde{u}_i\overline{\tau_{i,j}}}{\partial x_j} - \frac{\partial \overline{q_j}}{\partial x_j} - \frac{\partial q^t_j}{\partial x_j} + \overline{\dot{\omega}_T} \tag{75c}$$

where Y_k^ϕ, $\phi \in \{\ell, v\}$, is the species mass fraction for each phase. As for the 3-equation model, the species $\vec{J}_k^\phi$ and heat fluxes $\vec{q}$ use classical gradient approaches, the species flux making use of the phase species mass fraction Y_k^ϕ,

instead of the species mass fraction $Y_k = Y_k^v + Y_k^l$ for the 3-equation model. The fluid viscosity and the heat diffusion coefficient are calculated following the Chung *et al.* method [52] and mass diffusion coefficients are deduced from heat diffusivity by assuming a unity Lewis number (Le=1). The Soret and Dufour effects are neglected.

Turbulence Models. The same sub-grid scale (SGS) models as for the 3-equation model are used for the 4-equation model. The turbulent species flux is now written in terms of phase species mass fraction Y_k^ϕ:

$$\overline{J_{i,k}}^{t,\phi} = -\overline{\rho}\left(D_t \frac{\partial \widetilde{Y}_k^\phi}{\partial x_i}\right) \tag{76}$$

In the present work, only two-dimensional computations are led with the 4-equation model. Therefore, as for the 3-equation model, the SGS turbulent viscosity ν_t is modeled with the dynamic Smagorinsky model [57].

Phase change and combustion model. The species source term $\overline{\dot{\omega}_k^\phi}$ appears in equation (75a), which represents the variation of species k in phase ϕ. This variation can be due to phase change or to chemical reactions. Both phenomena are treated in the present work by means of stiff relaxation towards equilibrium. The computation is done through an operator-splitting strategy:

- after the hyperbolic transport step, chemical reactions are first treated, in very similar ways as for the 3-equation model. To achieve this, the global mixture composition is computed as $Y_k = Y_k^v + Y_k^l$. Then, the source term due to chemical reactions is computed globally as $\overline{\dot{\omega}_k} = \overline{\dot{\omega}_k^\ell} + \overline{\dot{\omega}_k^v}$, and its expression is given by equation (73). The energy source term is subsequently computed using equation (74);

- phase change is finally computed assuming an infinitely fast relaxation towards thermodynamic equilibrium between phases, providing the updated values for Y_k^v and Y_k^l.

It is worth mentioning that in practice, for the configurations studied in this work, *a posteriori* observations of the flow topology indicate that combustion only occurs within the gas phase.

6. Applications

The 3-equation model with the simplified equilibrium (Section 5.1) is now used for the three-dimensional simulation of the reactive configurations Mascotte G1 and A10. The main objective of these calculations is to assess the performance of the model on a realistic configuration with experimental data.

6.1. The MASCOTTE test bench

The Mascotte experimental configuration of ONERA [62], which has been extensively used for experimental studies of cryogenic combustion in collaboration with Laboratoire EM2C [3, 63], is considered here. The present simulations reproduce the operating cases G1 and A10 corresponding to subcritical pressure flames with respect to the oxygen critical pressure [3, 35, 36]. A single coaxial injector produces a liquid oxygen stream at low velocity (less than 10 m/s), surrounded by a high-velocity gaseous methane (for case G1) or hydrogen (for case A10) stream (more than 100 m/s). The chamber pressure is 46.9 bar for case G1 and 10 bar for case A10. The pressure is lower than the critical pressure of oxygen for both cases ($P_{C,\mathrm{O_2}}$=50.4 bar). However, in case G1, the reduced pressure for oxygen is close to 1 and surface tension is then expected to be much lower than for case A10. Table 2 details the inflow conditions. Oxygen is injected at 80 K, well below its critical value $T_{C,\mathrm{O_2}} = 154$ K and is in a liquid state, while the fuel, injected at 289 K is gaseous ($T_{C,\mathrm{H_2}} = 33$ K, $T_{C,\mathrm{CH_4}} = 190$ K). Under such conditions, the density of oxygen ($\rho_{\mathrm{O_2}} \approx 1100$ kg.m^{-3}) is much larger than that of hydrogen ($\rho_{\mathrm{H_2}} = 0.84$ kg.m^{-3}) and methane ($\rho_{\mathrm{CH_4}} = 35$ kg.m^{-3}). It should be noticed that the mixture is rich in fuel for both cases, the fuel being injected in excess.

Case	P_{ch} [MPa]	$T_{\mathrm{inj,fuel}}$ [K]	$T_{\mathrm{inj,O_2}}$ [K]	$\dot{m}_{\mathrm{fuel}}$ [g/s]	$\dot{m}_{\mathrm{O_2}}$ [g/s]	T_{R,O_2}	P_{R,O_2}
G1	4.68	289	80	101.2	43.9	0.52	0.93
A10	1.0	289	80	23.7	50	0.52	0.20

Table 2: Injection conditions for the Mascotte G1 and A10 cases. P_{ch} is the chamber pressure, T_{inj} is the injection temperature, $\dot{m}$ is the mass flow rate, $T_{R,O_2} = T_{\mathrm{inj}}/T_{C,O_2}$ is the reduced temperature and $P_{R,O_2} = P_{ch}/P_{C,O_2}$ is the reduced pressure.

6.2. Meshes, boundary conditions and numerical setup

Since the combustion chamber for cases A10 and G1 is the same and injectors are similar, only case G1 is detailed here, the grid distribution being conserved for the two cases. The simulation domain and the grid for case G1 are shown in figure 10. The chamber exactly corresponds to the one from the experiment, except that the outlet nozzle is replaced with a numerical outlet where the pressure is imposed. The mesh is refined just behind the lip, with 5 cells along its thickness. There are around 20 cells in each injector diameter. The grid contains about 2 000 000 nodes and 11 000 000 tetrahedrons.

Figure 10: Computational domain and grid distribution for the three-dimensional reactive simulation.

The walls are treated using adiabatic slip wall-law boundary condition [64]. The inlet and outlet conditions are both set with non-reflecting characteristic boundary conditions, with a relaxation on the pressure at the exit boundary condition [42]. Turbulent velocity fluctuations are superimposed to the bulk flow at the injection on both oxygen and fuel streams following turbulent injection profiles from prior pipe flow calculations and a Passot-Pouquet spectrum [65, 66].

6.3. Preliminary discussion on the model

Modeling the whole process that transforms the liquid oxygen injected into the gaseous oxygen mixed with hydrogen or methane to be ignited would require to couple a multifluid model to a disperse phase model, in order to address the atomization and treat the evaporation of the droplets. In the present work, the phase change is directly treated by the 3-equation model, through the phase equilibrium assumption.

The simplified strategy adopted here takes advantage of the strong mixing dynamics of the Mascotte configurations, which can be illustrated by the high Weber and Reynolds numbers characterizing such flows.

The Weber number We is a dimensionless number that compares the drag forces to the surface tension forces, computed as

$$\mathrm{We} = \frac{\rho_{v,0} l_0 (\Delta u)_0^2}{\sigma_0}, \tag{77}$$

where $\rho_{v,0}$ is the injected gas phase density, l_0 the typical length scale of the liquid jet (corresponding here to the nozzle diameter), $(\Delta u)_0$ the typical velocity difference responsible for the shear forces and σ_0 the surface tension coefficient. High Weber numbers are observed in flows where the surface tension has negligible effect compared to the drag force, so that the liquid phase cohesion cannot be maintained by the capillary forces. In the Mascotte A10 configuration, the Weber number is $\mathrm{We} \approx 28 \times 10^3$, following [36].

Another parameter that is important in the characterization of a liquid jet break-up regime is the Reynolds number for the liquid jet Re_ℓ. It is defined as

$$\mathrm{Re}_\ell = \frac{d_0 u_{0,\ell}}{\nu_\ell}, \tag{78}$$

which for the A10 configuration yields $\mathrm{Re}_\ell \approx 67 \times 10^3$. According to [67, 68], the regime corresponding to this set $(\mathrm{We}, \mathrm{Re}_\ell)$ corresponds to the fiber-type regime, in which the jet rapidly breaks-up into droplets of diameter several orders of magnitude below the nozzle diameter, see Figure 11. The obtained spray is then expected to be made up of small (low-inertia) droplets encountering strong temperature gradients due to the flame presence. It is thus reasonable

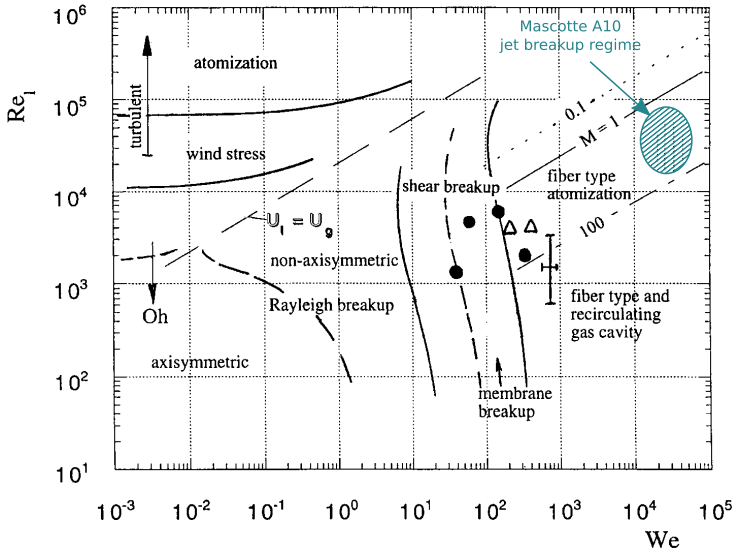

Figure 11: Characterization of the different spray regimes in the Re$_\ell$-We space. Image taken from [68]

to think that the spray representing the liquid phase undergoes stiff relaxation processes to the gas flow (regarding mechanical, thermal and thermodynamic non-equilibriums), so that the assumptions for the 3-equation model may not be too far from the actual flow behaviour.

6.4. Results for Case G1

Example of instantaneous fields of oxygen mass fraction, temperature, liquid volume fraction and stability criterion are shown in Fig. 12. The flame is characterized by a sudden termination at the distance $x \approx 12d$ from the injection plan, where d denotes the oxygen injector diameter. This topology, similar to the one observed for G2 flame operating at supercritical pressure [11, 60], is caused by a large scale recirculation zone at the end of the flame. A thin region of two-phase coexistence surrounds the high-density core, corresponding to the liquid-gas interface.

Results are now compared with the available experimental data from [35]. Figure 13 (bottom) shows an Abel's transform of experimental OH* mean emis-

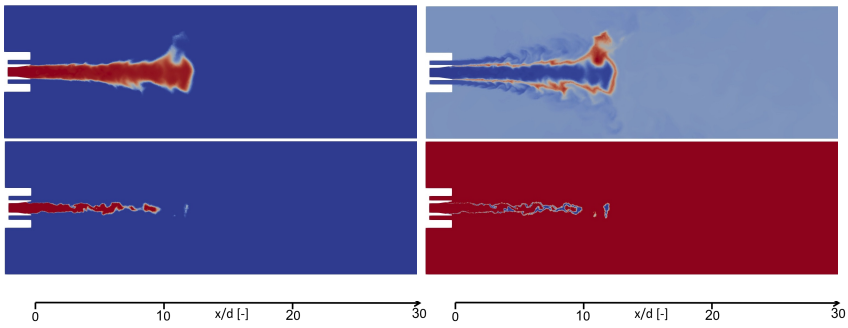

Figure 12: Instantaneous fields for the three-dimensional simulation of case G1 using the 3-equation model with simplified equilibrium. Top left: O_2 mass fraction Y_{O_2} (blue: 0, red: 1), top right: temperature (blue: 80 K, red: 3300 K), bottom left: liquid volume fraction z_ℓ (blue: 0, red: 1); bottom right: stability criterion (blue: unstable, red: stable).

sion, which qualitatively represents the flame location through the excited OH radical. In order to compare the flame position, a longitudinal cut of OH mass fraction extracted from the LES is shown on the upper part of the same figure. Good agreements are found, the initial and sudden flame opening are well retrieved as well as the closing position of the flame.

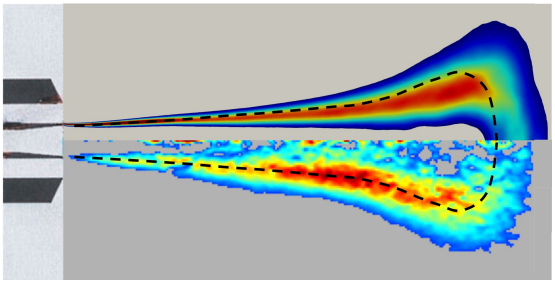

Figure 13: Comparison between Abel's transform of experimental OH* mean emission for case G1 [35] (bottom) and a longitudinal cut of mean OH mass fraction (Blue: 0.0035, red: 0.025) from LES (top). Dashed lines show the position of maximum OH* emission from experiments.

Liquid/vapor interface thickness. An estimation of the interface thickness δ_{zl} at a given distance x of the injector exit is computed from the maximum gradient

of the volume fraction z_ℓ:

$$\delta_{zl}(x) = \frac{1}{\max_y(\|\nabla z_\ell(x,y)\|)} \tag{79}$$

where the maximum is computed over a transverse profile of a longitudinal slice in the plan (x,y) of an instantaneous field. This method takes the minimum interface thickness along a profile and is well adapted for regions with properly defined liquid/vapor interfaces, but has a more qualitative meaning within the dispersed phase regions. However, it helps discriminating thin interfaces and dispersed phase parts of the flow. Figure 14 shows δ_{zl}/Δ_x, $\Delta_x \approx V_n^{1/3}$ being the characteristic cell size at the position of the interface and V_n the nodal volume. This interface thickness indicator remains close to 2 Δ_x along the inner dense jet. This shows that in this computation, a well described interface separates pure phases in most regions, while the presence of disperse interface "pockets" is relatively limited. The flow topology obtained is similar to the one described by [35], Figure 6.A.

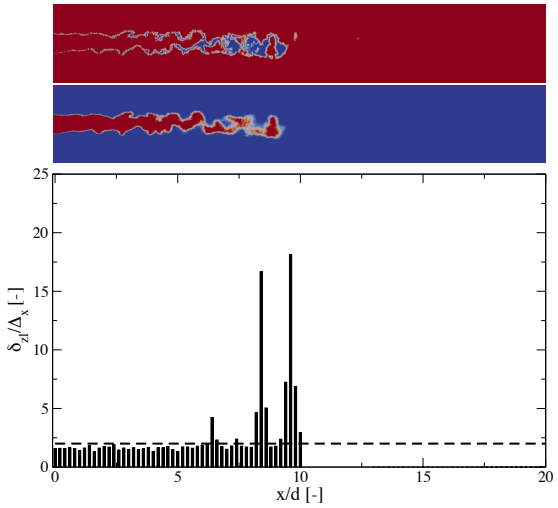

Figure 14: Case G1: liquid vapor interface thickness z_ℓ over the characteristic cell size Δ_x. Top: stability criterion (blue: unstable, red:stable) ; Middle: liquid volume fraction z_ℓ (blue: 0, red: 1) ; Bottom: δ_{z_ℓ}/Δ_x over the axial distance from the injector exit. The dashed line shows δ_{z_ℓ}/Δ_x=2.

6.5. Results for Case A10

Instantaneous fields of representative flow variables (temperature, O2, liquid volume fraction) are shown in figure 15. A turbulent diffusion flame is formed at the exit of the coaxial injector and surrounds the high density inner jet. As for case G1, the confinement of the flow by the walls produces a sudden opening of the flame at $x \approx 10d$ (d being the inner injector diameter). However, the flame being longer for case A10 compared with G1, the recirculation region is this time formed between the flame and the inner high density jet. Large-scale motions are noticeable further downstream. Such a flame topology is similar to the ones computed at supercritical pressure [11]. The region of two-phase coexistence is shown on the bottom field in figure 15. As the inner jet is destabilized, large scale regions are thermodynamically unstable. They disappear as the oxygen mixes and burns with the surrounding gases.

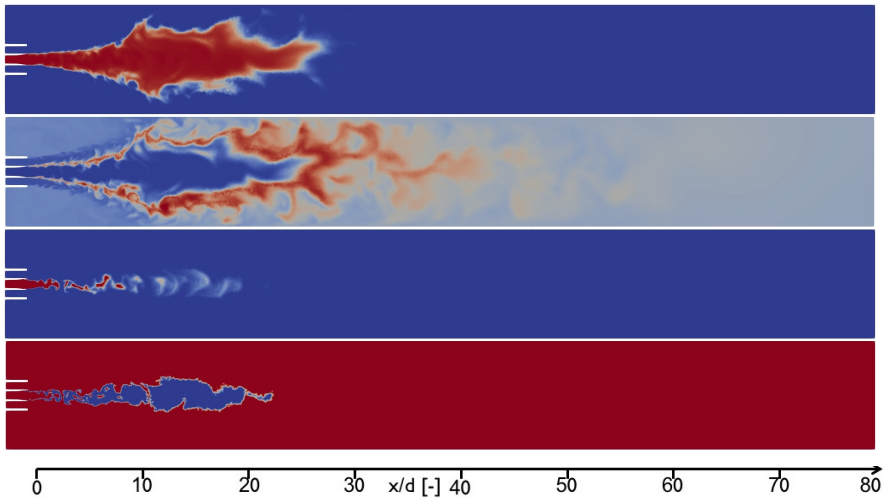

Figure 15: Instantaneous fields for the three-dimensional simulation using the 3-equation model with simplified equilibrium. From top to bottom: O_2 mass fraction Y_{O_2} (blue: 0, red: 1); temperature (blue: 80 K, red: 3500 K); liquid volume fraction z_ℓ (blue: 0, red: 1); stability criterion (blue: unstable, red:stable).

Results are compared with the available experimental data from [36]. Figure 16 (bottom) shows an Abel's transform of experimental OH^* mean emission,

which, again, qualitatively represents the flame location through the excited OH radical. In order to compare the flame position, a longitudinal slice of OH mass fraction is plotted in the upper half of the same figure. The initial opening of the flame is slightly under-estimated and the flame seems to be longer than in the experiment. There is an offset of approximatively 20% on the position of maximum opening. However, it seems that, despite the strong simplifications made in this simulation (no atomization, no surface tension, fast chemistry), the model can already give reasonable results for reactive liquid rocket engine flows.

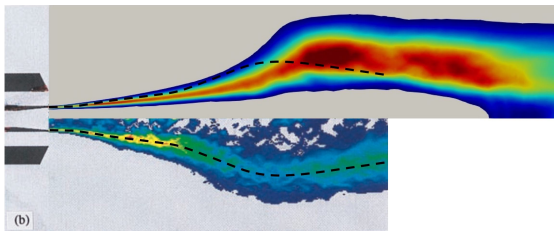

Figure 16: Comparison between Abel's transform of experimental OH* mean emission for case A10 [36] (bottom) and a mean longitudinal slice of OH mass fraction (blue: 0.006, red: 0.06) from LES (top). Dashed lines show the position of maximum OH* emission from experiments.

In this simplified modeling, two-phase regions of two different natures are observed in the flow (see Figure 15). Near the injector, a thin two-phase region separates liquid and gas phases and correspond to a diffuse liquid-gas interface representation. Conversely, downstream the liquid core, one may interpret the two-phase diffuse *pockets* that are surrounded by gas regions as liquid spray areas. Within such regions, the 3-equation model behaves like a simplified disperse phase model.

Besides, in this simulation, the dynamics are globally dominated by the turbulent fluxes, and the mixing between liquid and gas phases is mostly due to the subgrid-scale terms.

To assess the impact of the grid resolution, the simulation is performed on a coarser grid. The grid spacing is multiplied by a factor 1.5 over the whole domain, leading to a final grid size of 750,000 nodes and 4.3 millions tetrahedra.

Average fields of oxygen mass fraction, temperature and OH mass fraction are shown in Fig. 17 for the coarse grid and the current grid (referred as "fine"). The two grids show close results. However, the coarser mesh leads to a slightly shorter flame, certainly due to an excess of dissipation at the injector exit. From the weak difference between the two simulations, it is expected that the grid resolution has a minor impact on the average results, confirming the results on the fine grid. It indicates the departure observed between the simulation and the experiment could not be associated with a grid limitation.

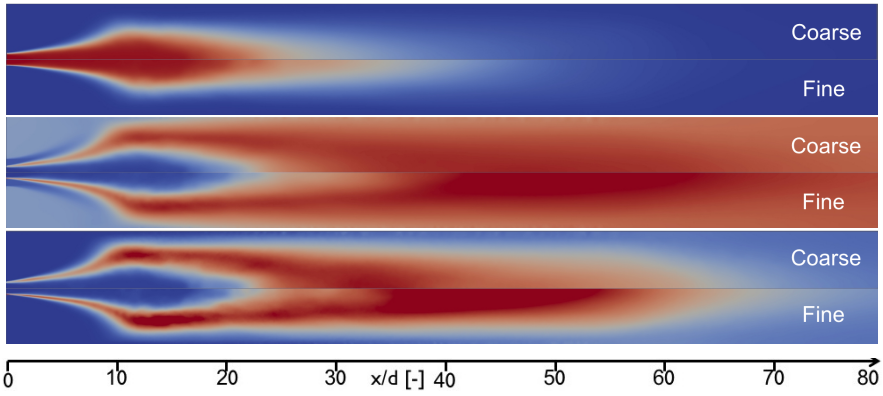

Figure 17: Average fields for the three-dimensional reactive simulation of case A10 with coarse and fine grids using the 3-equation model with simplified equilibrium. From top to bottom: O_2 mass fraction Y_{O_2} (blue: 0, red: 1); temperature (blue: 80 K, red: 2500 K); OH mass fraction Y_{OH} (blue: 0, red: 0.045).

Liquid/vapor interface thickness. As done previously for case G1, an estimation of the interface thickness δ_{zl} is computed from the maximum gradient of the volume fraction z_ℓ (Eq. 79). Figure 18 shows δ_{zl}/Δ_x computed along a longitudinal slice of an instantaneous field. As depicted before, two distinct behaviors are to be noticed. For $x < 7d$, the inner dense jet is not atomized and a thin diffuse liquid-gas interface is clearly identifiable. Its thickness is close to 2 Δ_x. Further downstream, as the liquid core is atomized, the two-phase region can be assimilated to a disperse phase one and its thickness is increasing.

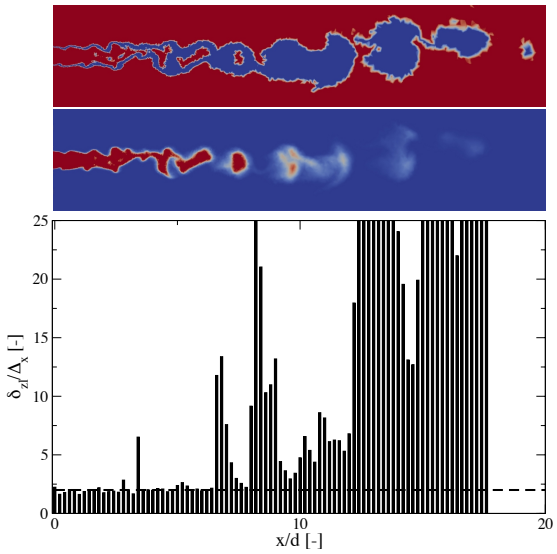

Figure 18: Case A10: liquid vapor interface thickness z_ℓ over the characteristic cell size Δ_x. Top: stability criterion (blue: unstable, red:stable) ; Middle: liquid volume fraction z_ℓ (blue: 0, red: 1) ; Bottom: δ_{z_ℓ}/Δ_x over the axial distance from the injector exit. The dashed line shows δ_{z_ℓ}/Δ_x=2.

Additional comments. The models tend to generate pressure fluctuations of large amplitude, as shown in the pressure scatter plot in figure 19a. These oscillations do not seem to notably affect the jets. This might be due to the very high frequency content of this noise, to which the inner jet is not sensitive. It should also be noted that this noise remains confined in the high density jet and does not notably pollute the rest of the chamber. Pressure fluctuations strongly increase at the transition from the interface to the pure liquid phase ($\rho \approx 950$ kg/m^3), and are mostly present within the liquid phase, as also evidenced by figure 19b.

7. Conclusions

This paper presented a global methodology to handle two-phase flows in a Taylor-Galerkin framework, extending a supercritical solver strategy to subcritical configurations. This is achieved by means of 3-equation and 4-equation

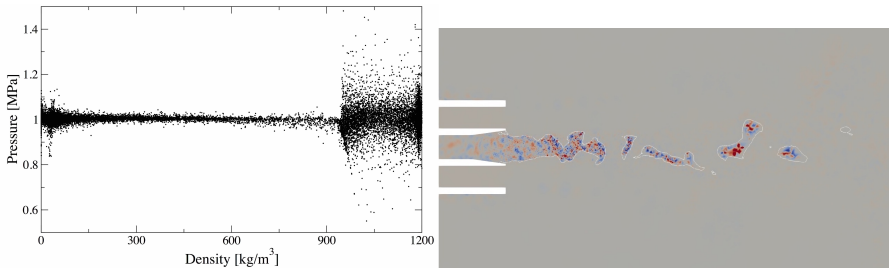

(a) Scatter plot of pressure against density (b) Instantaneous pressure field. Blue: 0.8 MPa, red: 1.2 MPa

Figure 19: Analyses of the pressure field. The scatter plot (a) shows that the spurious pressure oscillations mainly occur within the weakly compressible liquid phase, while the noise is relatively low within the interface $\rho \in [20, 50]$ kg/m^3 and the gas phase $\rho < 20$ kg/m^3. The instantaneous pressure field (b) is presented with the isocontour $\rho = 500$ kg/m^3, and displays the high spatial frequency content of spurious noise within the liquid phase.

multifluid models, using cubic equations of state for the thermodynamic closure. In order to compute the phase change, the multicomponent equilibrium computation techniques of [47] have been considered, and a simplified equilibrium formulation has been proposed, showing a behaviour close to the exact equilibrium for the thermodynamic regime of the Mascotte A10 configuration (ONERA).

The application to the simulation of two Mascotte configurations (G1 and A10) allowed to illustrate the behaviour of the multifluid models and their implementation on a realistic case. Case G1 is weakly subcritical, with a chamber pressure close to the critical pressure of oxygen (46.9 bar vs 50.4 bar), while case A10 operates at 10 bar. Results for case G1 are in very good agreement with experimental visualisations, while an over-prediction of the flame length around 20 % is observed for case A10. Despite the simplifications made in these computations, the results were in reasonable agreement with the experiments. These results are very encouraging regarding the application of the proposed methodology to liquid rocket engine simulations.

Future work will require to refine the two-phase flow modeling by incorporating a disperse spray modeling and coupling it to the multifluid model. Also, LES

subgrid-scale models should be derived for the specific treatment of the diffuse interface regions. The spurious pressure noise generation should be studied in order to limit its magnitude, while preserving a fully conservative formulation. Finally, it is will be necessary to add an interface sharpening method in order to prevent too strong diffusion of the interface region [69, 70].

Acknowledgments

The present work has been carried out within the ANR-14-CE22-011 project (SubSuperJet). This work was granted access to the HPC resources of IDRIS and CINES made available by GENCI (Grand Equipement National de Calcul Intensif) under the allocation A0042B06176. A part of this work was performed using HPC resources from the mesocentre computing center of Ecole CentraleSuplec and Ecole Normale Suprieure Paris-Saclay supported by CNRS and Rgion Ile-de-France.

The authors gratefully acknowledge Richard Saurel and Davy Nayigizente for fruitful discussions.

Appendix A. Thermodynamic tabulation for the single-component and approximate multicomponent equilibrium

Applying the *corresponding state principle*, the search for the two-phase equilibrium is reduced to a unique and universal computation for a given cubic EoS. In order to do this, instead of defining the usual set of reduced variables $T_r = {}^{T}/_{T_c}$, $P_r = {}^{P}/_{P_c}$ and $\rho_r = {}^{\rho}/_{\rho_c}$, we define the *reduced-saturation* (Rsat) variables:

$$\nu \triangleq \frac{1}{\bar{b}\rho}, \qquad \pi \triangleq \frac{P\bar{b}}{\bar{r}T}, \qquad \theta \triangleq \frac{\bar{a}(T)}{\bar{b}\bar{r}T}. \tag{A.1}$$

where ν is called the Rsat-volume, π the Rsat-pressure, and θ the Rsat-temperature (although it has the dimension of the inverse of a temperature).

The cubic EoS may then be rewritten under the form:

$$\pi(\nu,\theta) = \frac{1}{\nu-1} - \frac{\theta}{\nu^2+\varepsilon_1\nu-\varepsilon_2}, \tag{A.2}$$

and the fugacity coefficient expression also reduces to:

$$\varphi(\nu,\theta) = \frac{1}{\pi(\nu-1)}\left[\frac{2\nu+\varepsilon_1-\varepsilon_{12}}{2\nu+\varepsilon_1+\varepsilon_{12}}\right]^{\left(\frac{\theta}{\varepsilon_{12}}\right)} \exp\left(\pi\nu-1\right). \tag{A.3}$$

This shows that the search for the saturation pressure takes the same form for any species. Indeed, it appears in equations (A.2) and (A.3) that only the EoS-specific parameters are left: the species-specific parameters do no longer appear.

For a given mixture at a given temperature, θ is known. The determination of the Rsat-pressure π at saturation requires to find π^{sat} such that:

$$\varphi\big(\pi^{\mathrm{sat}},\nu^{\mathrm{min}}(\pi^{\mathrm{sat}},\theta)\big) = \varphi\big(\pi^{\mathrm{sat}},\nu^{\mathrm{max}}(\pi^{\mathrm{sat}},\theta)\big), \tag{A.4}$$

where $\nu^{\mathrm{min}}(\pi,\theta)$ and $\nu^{\mathrm{max}}(\pi,\theta)$ are the minimum and maximum positive roots of the reduced cubic equation

$$\nu^3 + \left[\varepsilon_1 - 1 - \frac{1}{\pi}\right]\nu^2 + \left[\frac{\theta-\varepsilon_1}{\pi} - (\varepsilon_1+\varepsilon_2)\right]\nu + \left[\varepsilon_2\left(\frac{1}{\pi}+1\right) - \frac{\theta}{\pi}\right] = 0. \tag{A.5}$$

Note that for $\pi = \pi^{\mathrm{sat}}(\theta)$, one has

$$\begin{cases} \nu^{\min}(\pi^{\mathrm{sat}}, \theta) = \nu_\ell(\theta) = \dfrac{1}{\bar{b}\rho_\ell}, & \text{(A.6a)} \\ \nu^{\max}(\pi^{\mathrm{sat}}, \theta) = \nu_v(\theta) = \dfrac{1}{\bar{b}\rho_v}. & \text{(A.6b)} \end{cases}$$

The following notation is used:

$$\begin{cases} \varphi_\ell(\pi) = \varphi\big(\pi, \nu^{\min}(\pi, \theta)\big), & \text{(A.7a)} \\ \varphi_v(\pi) = \varphi\big(\pi, \nu^{\max}(\pi, \theta)\big). & \text{(A.7b)} \end{cases}$$

To solve this problem, a Newton-Raphson procedure may be used. The function to be canceled is given by

$$f_\theta : \pi \mapsto \varphi_\ell(\pi, \theta) - \varphi_v(\pi, \theta), \tag{A.8}$$

the derivative of which is

$$f'_\theta(\pi) = \left(\nu^{\min}(\pi, \theta) - \frac{1}{\pi}\right)\varphi_\ell(\pi, \theta) - \left(\nu^{\max}(\pi, \theta) - \frac{1}{\pi}\right)\varphi_v(\pi, \theta). \tag{A.9}$$

If $\pi^{(k)}$ is the k^{th} iterate, its update reads

$$\pi^{(k+1)} = \pi^{(k)} - \frac{f_\theta(\pi^{(k)})}{f'_\theta(\pi^{(k)})} = 2\pi^{(k)} - \frac{\varphi_\ell(\pi^{(k)}, \theta) - \varphi_v(\pi^{(k)}, \theta)}{\nu^{\min}(\pi^{(k)}, \theta)\varphi_\ell(\pi^{(k)}, \theta) - \nu^{\max}(\pi^{(k)}, \theta)\varphi_v(\pi^{(k)}, \theta)}. \tag{A.10}$$

The solver iterates until the relative difference of the fugacity coefficients is under a tolerance value

$$\frac{\varphi_\ell - \varphi_v}{\max(\varphi_\ell, \varphi_v)} < \epsilon_{\mathrm{tol}}. \tag{A.11}$$

In practice, this saturation computation is processed offline once and for all, for any component, for a given EoS. It is then stored in a table that contains $\theta, \nu_\ell(\theta), \nu_v(\theta)$, and also $\frac{\mathrm{d}\nu_\ell}{\mathrm{d}\theta}$, $\frac{\mathrm{d}\nu_v}{\mathrm{d}\theta}$, to allow cubic polynomial interpolation. There is no need to store $\pi(\theta)$ since the saturation pressure can be directly computed from the EoS knowing the temperature and phases densities.

In order to evaluate $P^{\mathrm{sat}}(T)$, $\rho_\ell^{\mathrm{sat}}(T)$ and $\rho_v^{\mathrm{sat}}(T)$, the reduced temperature $\theta(T, \underline{\boldsymbol{Y}})$ is computed and the table is directly read.

Appendix B. Jacobian terms and speed of sound for the 4-equation model

Jacobian terms

The coefficients ζ and ξ_i^ℓ, ξ_i^v can be obtained by writing the mixture sensible energy and specific volume differentials:

$$\mathrm{d}e_s = y_\ell \,\mathrm{d}e_\ell + y_v \,\mathrm{d}e_v + e_\ell \,\mathrm{d}y_\ell + e_v \,\mathrm{d}y_v \tag{B.1a}$$

$$\mathrm{d}v = y_\ell \,\mathrm{d}v_\ell + y_v \,\mathrm{d}v_v + v_\ell \,\mathrm{d}y_\ell + v_v \,\mathrm{d}y_v, \tag{B.1b}$$

where the sensible energy and volume of each phase vary as

$$\mathrm{d}e_\phi = \left(v_\phi\beta_\phi P - v_\phi\alpha_\phi T\right)\mathrm{d}P + \left(c_{p,\phi} - v_\phi\alpha_\phi P\right)\mathrm{d}T + \sum_{i=1}^{N_s} e_{\phi,i}\,\mathrm{d}\left(\frac{Y_i^\phi}{y_\phi}\right) \tag{B.2a}$$

$$\mathrm{d}v_\phi = -v_\phi\beta_\phi\,\mathrm{d}P + v_\phi\alpha_\phi\,\mathrm{d}T + \sum_{i=1}^{N_s} v_{\phi,i}\,\mathrm{d}\left(\frac{Y_i^\phi}{y_\phi}\right). \tag{B.2b}$$

Noting that

$$y_\phi = \sum_{i=1}^{N_s} Y_i^\phi, \tag{B.3}$$

equations (B.2) become

$$\mathrm{d}e_\phi = \left(v_\phi\beta_\phi P - v_\phi\alpha_\phi T\right)\mathrm{d}P + \left(v_\phi C_{p,\phi} - v_\phi\alpha_\phi P\right)\mathrm{d}T + \sum_{i=1}^{N_s} \frac{e_{\phi,i} - e_\phi}{y_\phi}\,\mathrm{d}Y_i^\phi$$

$$\mathrm{d}v_\phi = -v_\phi\beta_\phi\,\mathrm{d}P + v_\phi\alpha_\phi\,\mathrm{d}T + \sum_{i=1}^{N_s} \frac{v_{\phi,i} - v_\phi}{y_\phi}\,\mathrm{d}Y_i^\phi.$$

(B.4a)

(B.4b)

Recasting this result into (B.1), one gets

$$\mathrm{d}e_s = \frac{1}{\rho}\left[\beta_{\mathrm{mix}}P - \alpha_{\mathrm{mix}}T\right]\mathrm{d}P + \frac{1}{\rho}\left[C_{p,\mathrm{mix}} - \alpha_{\mathrm{mix}}P\right]\mathrm{d}T + \sum_{i=1}^{N_s} e_{\ell,i}\,\mathrm{d}Y_i^{\ell} + \sum_{i=1}^{N_s} e_{v,i}\,\mathrm{d}Y_i^{v}$$

$$\mathrm{d}v = -\frac{1}{\rho}\beta_{\mathrm{mix}}\,\mathrm{d}P + \frac{1}{\rho}\alpha_{\mathrm{mix}}\,\mathrm{d}T + \sum_{i=1}^{N_s} v_{\ell,i}\,\mathrm{d}Y_i^{\ell} + \sum_{i=1}^{N_s} v_{v,i}\,\mathrm{d}Y_i^{v} \tag{B.5a}$$

(B.5b)

Then, from (B.5b), since, $\mathrm{d}v = -\frac{1}{\rho^2}\,\mathrm{d}\rho$, the temperature differential can be written as

$$\mathrm{d}T = -\frac{1}{\rho\alpha_{\mathrm{mix}}}\,\mathrm{d}\rho + \frac{\beta_{\mathrm{mix}}}{\alpha_{\mathrm{mix}}}\,\mathrm{d}P - \sum_{i=1}^{N_s}\frac{\rho v_{\ell,i}}{\alpha_{\mathrm{mix}}}\,\mathrm{d}Y_i^{\ell} - \sum_{i=1}^{N_s}\frac{\rho v_{v,i}}{\alpha_{\mathrm{mix}}}\,\mathrm{d}Y_i^{v} \tag{B.6}$$

Injecting this relation into the sensible energy differential (B.5a), it yields

$$\begin{aligned}\mathrm{d}e_s =& \frac{1}{\rho}\left[C_{p,\mathrm{mix}}\frac{\beta_{\mathrm{mix}}}{\alpha_{\mathrm{mix}}} - \alpha_{\mathrm{mix}}T\right]\mathrm{d}P + \frac{1}{\rho^2}\left[P - \frac{C_{p,\mathrm{mix}}}{\alpha_{\mathrm{mix}}}\right]\mathrm{d}\rho \\ &- \frac{C_{p,\mathrm{mix}}}{\alpha_{\mathrm{mix}}}\left[\sum_{i=1}^{N_s} v_{\ell,i}\,\mathrm{d}Y_i^{\ell} + \sum_{i=1}^{N_s} v_{v,i}\,\mathrm{d}Y_i^{v}\right] + \sum_{i=1}^{N_s} h_{\ell,i}\,\mathrm{d}Y_i^{\ell} + \sum_{i=1}^{N_s} h_{v,i}\,\mathrm{d}Y_i^{v}\end{aligned} \tag{B.7}$$

which corresponds to

$$\begin{aligned}\mathrm{d}(\rho e_s) =& \left(C_{p,\mathrm{mix}}\frac{\beta_{\mathrm{mix}}}{\alpha_{\mathrm{mix}}} - \alpha_{\mathrm{mix}}T\right)\mathrm{d}P + \left[h_s - \frac{C_{p,\mathrm{mix}}}{\alpha_{\mathrm{mix}}}\right]\mathrm{d}\rho \\ &- \frac{C_{p,\mathrm{mix}}}{\alpha_{\mathrm{mix}}}\left[\sum_{i=1}^{N_s} v_{\ell,i}\rho\,\mathrm{d}Y_i^{\ell} + \sum_{i=1}^{N_s} v_{v,i}\rho\,\mathrm{d}Y_i^{v}\right] + \sum_{i=1}^{N_s} h_{\ell,i}\rho\,\mathrm{d}Y_i^{\ell} + \sum_{i=1}^{N_s} h_{v,i}\rho\,\mathrm{d}Y_i^{v}\end{aligned} \tag{B.8}$$

and

$$\mathrm{d}(\rho e_s) = \left(C_{p,\mathrm{mix}}\frac{\beta_{\mathrm{mix}}}{\alpha_{\mathrm{mix}}} - \alpha_{\mathrm{mix}}T\right)\mathrm{d}P + \sum_{\phi\in\{\ell,v\}}\sum_{i=1}^{N_s}\left(h_{\phi,i} - \frac{C_{p,\mathrm{mix}}}{\alpha_{\mathrm{mix}}}v_{\phi,i}\right)\mathrm{d}\left(\rho Y_i^{\phi}\right). \tag{B.9}$$

Finally, this provides the values of the coefficients:

$$\begin{cases} \zeta = \dfrac{1}{C_{p,\mathrm{mix}}\frac{\beta_{\mathrm{mix}}}{\alpha_{\mathrm{mix}}} - \alpha_{\mathrm{mix}} T} & \text{(B.10a)} \\ \xi_i^{\phi} = h_{\phi,i} - \dfrac{C_{p,\mathrm{mix}}}{\alpha_{\mathrm{mix}}} v_{\phi,i} & \text{(B.10b)} \end{cases}$$

Speed of sound

The Jacobian matrix having the same form as for the previous systems, the speed of sound reads:

$$c^2 = \left.\frac{\partial P}{\partial \rho}\right|_{s,\underline{\boldsymbol{Y}}}, \tag{B.11}$$

except that now, the mass fractions $\underline{\boldsymbol{Y}} = \left[Y_1^{\ell}, \cdots, Y_{N_s}^{\ell}, Y_1^{v}, \cdots, Y_{N_s}^{v}\right]^t$ of the components in the liquid and the vapour phases are fixed. Note that the liquid mass fraction y_ℓ is then also constant.

In this respect, one can write the differential of the mixture mass-specific volume at constant composition:

$$\mathrm{d}v = \mathrm{d}\big(y_\ell v_\ell + (1-y_\ell)v_v\big) = y_\ell\,\mathrm{d}v_\ell + (1-y_\ell)\,\mathrm{d}v_v. \tag{B.12}$$

Expanding the differentials of the liquid and vapour specific volumes, at constant composition, on has

$$\begin{aligned} \mathrm{d}v &= \big(y_\ell v_\ell \alpha_\ell + (1-y_\ell)v_v\alpha_v\big)\,\mathrm{d}T - \big(y_\ell v_\ell \beta_\ell + (1-y_\ell)v_v\beta_v\big)\,\mathrm{d}P, & \text{(B.13)} \\ &= v\alpha_{\mathrm{mix}}\,\mathrm{d}T - v\beta_{\mathrm{mix}}\,\mathrm{d}P, & \text{(B.14)} \end{aligned}$$

so that

$$\mathrm{d}T = -\frac{1}{\rho\alpha_{\mathrm{mix}}}\,\mathrm{d}\rho + \frac{\beta_{\mathrm{mix}}}{\alpha_{\mathrm{mix}}}\,\mathrm{d}P. \tag{B.15}$$

Similarly, the mixture entropy differential at constant composition reads

$$\mathrm{d}s = y_\ell\,\mathrm{d}s_\ell + (1-y_\ell)\,\mathrm{d}s_v, \tag{B.16}$$

which expands to

$$\begin{aligned} \mathrm{d}s &= \left[y_\ell\frac{c_{p,\ell}}{T} + (1-y_\ell)\frac{c_{p,v}}{T}\right]\mathrm{d}T - \big[y_\ell v_\ell\alpha_\ell + (1-y_\ell)v_v\alpha_v\big]\,\mathrm{d}P, & \text{(B.17)} \\ &= \frac{\bar{c_{\mathrm{p}}}}{T}\,\mathrm{d}T - \frac{\alpha_{\mathrm{mix}}}{\rho}\,\mathrm{d}P, & \text{(B.18)} \end{aligned}$$

with $\bar{c_{\mathrm{p}}} = y_\ell c_{p,\ell} + (1-y_\ell)c_{p,v}$. Casting (B.15) into (B.18) finally yields:

$$\mathrm{d}s = -\frac{1}{\rho\alpha_{\mathrm{mix}}}\frac{\bar{c_{\mathrm{p}}}}{T}\,\mathrm{d}\rho + \left[-\frac{\alpha_{\mathrm{mix}}}{\rho} + \frac{\bar{c_{\mathrm{p}}}}{T}\frac{\beta_{\mathrm{mix}}}{\alpha_{\mathrm{mix}}}\right]\mathrm{d}P, \tag{B.19}$$

hence the speed of sound for the 4-equation system:

$$c^2 = \frac{\bar{c_{\mathrm{p}}}}{\rho\beta_{\mathrm{mix}}\bar{c_{\mathrm{p}}} - \alpha_{\mathrm{mix}}^2 T} \tag{B.20}$$

Appendix C. Characteristic boundary conditions

When dealing with compressible flows, it is particularly important to apply properly the boundary conditions. Indeed, as the boundary conditions are imposed by modifying the conservative quantities at the boundary nodes, it is necessary that such modifications be applied on the incoming waves only to prevent any spurious pressure oscillations at the boundaries, as discussed in [42]. This is even more important when low dissipation schemes such as TTG schemes are used.

Considering the boundary frame $\mathcal{R}_{\mathrm{B}} = (\vec{n}, \vec{t}_1, \vec{t}_2)$, with $\vec{n}$ the unit vector normal to the boundary and $\vec{t}_{1,2}$ tangent unit vectors that complete the orthonormal basis, the 3-equation model is written in a pseudo-linear form:

$$\frac{\partial \mathbf{U}}{\partial t} + \mathbf{J}^{\vec{n}} \cdot \left(\vec{\nabla}\mathbf{U}\cdot\vec{n}\right) + \mathbf{J}^{\vec{t}_1} \cdot \left(\vec{\nabla}\mathbf{U}\cdot\vec{t}_1\right) + \mathbf{J}^{\vec{t}_2} \cdot \left(\vec{\nabla}\mathbf{U}\cdot\vec{t}_2\right) = 0 \tag{C.1}$$

with $\mathbf{J}^{\vec{n}}(\mathbf{U}) = \mathcal{J}(\mathbf{U})\cdot\vec{n}$. As the boundary conditions generally consist in prescribing values for the primitive variables $\mathbf{V} = \begin{bmatrix}\rho Y_1 & \cdots & \rho Y_{N_s} & u_{\vec{n}} & u_{\vec{t}_1} & u_{\vec{t}_2} & P\end{bmatrix}^t$, it is useful to provide the *transformation matrices* $\mathcal{T}_{\mathbf{VU}}$ and $\mathcal{T}_{\mathbf{UV}} = \mathcal{T}_{\mathbf{VU}}^{-1}$ to change basis between the conservative and primitive variables. For any thermodynamic closure (whether for a single-phase state or two-phase equilibrium state), it reads:

$$\mathcal{T}_{\mathbf{VU}} = \left[\left.\frac{\partial \mathbf{U}_i}{\partial \mathbf{V}_j}\right|_{\mathbf{V}_{k\neq j}}\right] = \begin{bmatrix} 1 & \cdots & 0 & 0 & 0 & 0 & 0 \\ \vdots & \ddots & \vdots & \vdots & \vdots & \vdots & \vdots \\ 0 & \cdots & 1 & 0 & 0 & 0 & 0 \\ u_{\vec{n}} & \cdots & u_{\vec{n}} & \rho & 0 & 0 & 0 \\ u_{\vec{t}_1} & \cdots & u_{\vec{t}_1} & 0 & \rho & 0 & 0 \\ u_{\vec{t}_2} & \cdots & u_{\vec{t}_2} & 0 & 0 & \rho & 0 \\ (e_c+\xi_1) & \cdots & (e_c+\xi_{N_s}) & \rho u_{\vec{n}} & \rho u_{\vec{t}_1} & \rho u_{\vec{t}_2} & \frac{1}{\zeta} \end{bmatrix}. \tag{C.2}$$

Here, $u_{\vec{n}}$, $u_{\vec{t}_1}$ and $u_{\vec{t}_2}$ denote respectively the velocity components along vectors $\vec{n}, \vec{t}_1$ and $\vec{t}_2$

The diagonalization of the Jacobian matrix along the boundary normal $\mathbf{J}^{\vec{n}}$ yields the *characteristic form* of the hyperbolic system. This writes

$$\mathbf{J}^{\vec{n}}_{\mathbf{V}} = \mathcal{T}_{\mathbf{WV}}\, \mathbf{J}^{\vec{n}}_{\mathbf{W}}\, \mathcal{T}_{\mathbf{VW}}, \tag{C.3}$$

where, for any thermodynamic closure, $\mathbf{J}^{\vec{n}}_{\mathbf{W}} = \mathrm{diag}(u_{\vec{n}} \;\; \cdots \;\; u_{\vec{n}} \;\; u_{\vec{n}} - c \;\; u_{\vec{n}} + c)$ is the Jacobian matrix in the characteristic variables $\mathbf{W}$. The matrices of left and right eigenvectors are referred to as the *transformation matrices*, allowing to change basis between the primitive and characteristic variables:

$$\frac{\partial \mathbf{W}}{\partial \mathbf{V}} = \mathcal{T}_{\mathbf{VW}} \qquad ; \qquad \frac{\partial \mathbf{V}}{\partial \mathbf{W}} = \mathcal{T}_{\mathbf{WV}} = \mathcal{T}^{-1}_{\mathbf{VW}} \tag{C.4}$$

One has

$$\mathcal{T}_{\mathbf{VW}} = \mathcal{T}^{-1}_{\mathbf{WV}} = \begin{bmatrix} 1 & \cdots & 0 & {}^{-Y_1}\!/_{c^2} & 0 & 0 & 0 \\ \vdots & \ddots & \vdots & \vdots & \vdots & \vdots & \vdots \\ 0 & \cdots & 1 & {}^{-Y_{N_s}}\!/_{c^2} & 0 & 0 & 0 \\ 0 & \cdots & 0 & 0 & 1 & 0 & 0 \\ 0 & \cdots & 0 & 0 & 0 & 1 & 0 \\ 0 & \cdots & 0 & {}^{1}\!/_{\rho c} & 0 & 0 & -1 \\ 0 & \cdots & 0 & {}^{1}\!/_{\rho c} & 0 & 0 & 1 \end{bmatrix}. \tag{C.5}$$

One observes that the characteristic form of the three-equation model for a two-phase mixture state at equilibrium is similar to the one of the Euler equations. Yet, ad-hoc thermodynamic coefficients χ_k, ζ and c (the speed of sound) must be computed, according to (51), (52) and (43) in the case of a two-phase thermodynamic state.

Using these developments, the application of the characteristic boundary conditions can be summarized as follows:

1. compute the residual in conservative variables corresponding to the hyperbolic transport across the inner domain,
2. at the boundary nodes, transform the obtained residual from conservative to characteristic variables using the transformation matrices,

3. cancel the characteristic components carried by incoming waves through the boundary,
4. prescribe these characteristic components to values that correspond to the desired boundary condition behaviour [42],
5. transform the obtained characteristic variations back to the residual in conservative variables and apply it.

References

[1] J. C. Oefelein, V. Yang, Modeling high-pressure mixing and combustion processes in liquid rocket engines, Journal of Propulsion and Power 14 (5) (1998) 843–857.

[2] V. Yang, Modeling of supercritical vaporization, mixing, and combustion processes in liquid-fueled propulsion systems, Proceedings of the Combustion Institute 28 (1) (2000) 925–942. doi:http://dx.doi.org/10.1016/S0082-0784(00)80299-4.

[3] S. Candel, M. Juniper, G. Singla, P. Scouflaire, C. Rolon, Structure and dynamics of cryogenic flames at supercritical pressure, Combustion Science and Technology 178 (1-3) (2006) 161–192.

[4] H. Müller, C. A. Niedermeier, J. Matheis, M. Pfitzner, S. Hickel, Large-eddy simulation of nitrogen injection at trans- and supercritical conditions, Physics of Fluids 28 (1) (2016) 015102. doi:10.1063/1.4937948.

[5] D.-Y. Peng, D. B. Robinson, A new two-constant equation of state, Industrial & Engineering Chemistry Fundamentals 15 (1) (1976) 59–64.

[6] G. Soave, Equilibrium constants from a modified Redlich-Kwong equation of state, Chemical Engineering Science 27 (6) (1972) 1197 – 1203. doi:https://doi.org/10.1016/0009-2509(72)80096-4.
URL http://www.sciencedirect.com/science/article/pii/0009250972800964

[7] J. C. Oefelein, Mixing and combustion of cryogenic oxygen-hydrogen shear-coaxial jet flames at supercritical pressure, Combustion Science and Technology 178 (1-3) (2006) 229–252. doi:10.1080/00102200500325322.

[8] N. Zong, V. Yang, Cryogenic fluid jets and mixing layers in transcritical and supercritical environments, Combustion science and technology 178 (1-3) (2006) 193–227.

[9] L. Hakim, A. Ruiz, T. Schmitt, M. Boileau, G. Staffelbach, S. Ducruix, B. Cuenot, S. Candel, Large eddy simulations of multiple transcritical coaxial flames submitted to a high-frequency transverse acoustic modulation, Proceedings of the Combustion Institute 35 (2) (2015) 1461 – 1468. doi:https://doi.org/10.1016/j.proci.2014.05.142.

[10] A. Urbano, Q. Douasbin, L. Selle, G. Staffelbach, B. Cuenot, T. Schmitt, S. Ducruix, S. Candel, Study of flame response to transverse acoustic modes from the les of a 42-injector rocket engine, Proceedings of the Combustion Institute 36 (2) (2017) 2633–2639. doi:10.1016/j.proci.2016.06.042.

[11] T. Schmitt, Large-eddy simulations of the Mascotte test cases operating at supercritical pressure (submitted), Journal of Flow, Turbulence and Combustion.

[12] S. Osher, J. A. Sethian, Fronts propagating with curvature-dependent speed: algorithms based on Hamilton-Jacobi formulations, Journal of computational physics 79 (1) (1988) 12–49.

[13] E. Olsson, G. Kreiss, S. Zahedi, A conservative level set method for two phase flow II, Journal of Computational Physics 225 (1) (2007) 785–807.

[14] O. Desjardins, V. Moureau, H. Pitsch, An accurate conservative level-set/ghost-fluid method for simulating turbulent atomization, Journal of Computational Physics 227 (18) (2008) 8395–8416.

[15] C. W. Hirt, B. D. Nichols, Volume of fluid (VOF) method for the dynamics of free boundaries, Journal of computational physics 39 (1) (1981) 201–225.

[16] J. E. Pilliod Jr, E. G. Puckett, Second-order accurate volume-of-fluid algorithms for tracking material interfaces, Journal of Computational Physics 199 (2) (2004) 465–502.

[17] J. Glimm, E. Isaacson, D. Marchesin, O. McBryan, Front tracking for hyperbolic systems, Advances in Applied Mathematics 2 (1) (1981) 91–119.

[18] S. Popinet, S. Zaleski, A front-tracking algorithm for accurate representation of surface tension, International Journal for Numerical Methods in Fluids 30 (6) (1999) 775–793.

[19] H. Terashima, G. Tryggvason, A front-tracking/ghost-fluid method for fluid interfaces in compressible flows, Journal of Computational Physics 228 (11) (2009) 4012–4037.

[20] R. P. Fedkiw, T. Aslam, B. Merriman, S. Osher, A non-oscillatory Eulerian approach to interfaces in multimaterial flows (the ghost fluid method), Journal of computational physics 152 (2) (1999) 457–492.

[21] J. D. van der Waals, The thermodynamic theory of capillarity under the hypothesis of a continuous variation of density, Journal of Statistical Physics 20 (1979) 200–244. doi:10.1007/BF01011514.

[22] D. Jamet, Etude des potentialités de la théorie du second gradient pour la simulation numérique directe des écoulements liquide-vapeur avec changement de phase, Ph.D. thesis, Châtenay-Malabry, Ecole centrale de Paris (1998).

[23] M. Baer, J. Nunziato, A two-phase mixture theory for the deflagration-to-detonation transition (ddt) in reactive granular materials, International journal of multiphase flow 12 (6) (1986) 861–889.

[24] A. Kapila, R. Menikoff, J. Bdzil, S. Son, D. S. Stewart, Two-phase modeling of deflagration-to-detonation transition in granular materials: reduced equations, Physics of fluids 13 (10) (2001) 3002–3024.

[25] G. Allaire, S. Clerc, S. Kokh, A five-equation model for the simulation of interfaces between compressible fluids, Journal of Computational Physics 181 (2) (2002) 577–616.

[26] A. Murrone, H. Guillard, A five equation reduced model for compressible two phase flow problems, Journal of Computational Physics 202 (2) (2005) 664–698.

[27] S. Le Martelot, R. Saurel, B. Nkonga, Towards the direct numerical simulation of nucleate boiling flows, International Journal of Multiphase Flow 66 (2014) 62–78.

[28] R. Saurel, R. Abgrall, A multiphase Godunov method for compressible multifluid and multiphase flows, Journal of Computational Physics 150 (2) (1999) 425–467.

[29] A. Chiapolino, P. Boivin, R. Saurel, A simple phase transition relaxation solver for liquid-vapor flows, International Journal for Numerical Methods in Fluids 83 (7) (2016) 583–605.

[30] L. Qiu, R. D. Reitz, Simulation of supercritical fuel injection with condensation, International Journal of Heat and Mass Transfer 79 (2014) 1070–1086.

[31] J. Matheis, S. Hickel, Multi-component vapor-liquid equilibrium model for LES of high-pressure fuel injection and application to ECN spray A, International Journal of Multiphase Flow 99 (2018) 294–311.

[32] C. Traxinger, M. Pfitzner, S. Baab, G. Lamanna, B. Weigand, Experimental and numerical investigation of phase separation due to multicomponent mixing at high-pressure conditions, Physical Review Fluids 4 (7) (2019) 074303.

[33] P. C. Ma, H. Wu, T. Jaravel, L. Bravo, M. Ihme, Large-eddy simulations of transcritical injection and auto-ignition using diffuse-interface method and finite-rate chemistry, Proceedings of the Combustion Institute 37 (3) (2019) 3303–3310.

[34] C. Traxinger, J. Zips, M. Pfitzner, Single-phase instability in non-premixed flames under liquid rocket engine relevant conditions, Journal of Propulsion and Power 35 (4) (2019) 675–689.

[35] G. Singla, P. Scouflaire, C. Rolon, S. Candel, Transcritical oxygen/transcritical or supercritical methane combustion, Proceedings of the combustion institute 30 (2) (2005) 2921–2928.

[36] S. Candel, G. Herding, R. Synder, P. Scouflaire, C. Rolon, L. Vingert, M. Habiballah, F. Grisch, M. Péalat, P. Bouchardy, D. Stepowski, A. Cessou, P. Colin, Experimental investigation of shear coaxial cryogenic jet flames, Journal of Propulsion and Power 14 (5) (1998) 826–834. doi:10.2514/2.5346.

[37] J. Donea, A Taylor–Galerkin method for convective transport problems, International Journal for Numerical Methods in Engineering 20 (1) (1984) 101–119.

[38] J. Donea, A. Huerta, Finite element methods for flow problems, John Wiley & Sons, 2003.

[39] O. Colin, A finite element operator for diffusion terms in AVBP, Tech. rep., IFP (2003).

[40] M. Barret, E. Faucher, J.-M. Hérard, Schemes to compute unsteady flashing flows, AIAA journal 40 (5) (2002) 905–913.

[41] T. Schmitt, Simulation des grandes échelles de la combustion turbulente à pression supercritique, Ph.D. thesis, INP Toulouse, thèse de doctorat dirigée par Cuenot, Bénédicte et Selle, Laurent Dynamique des fluides Toulouse, INPT 2009 (2009).
URL http://www.theses.fr/2009INPT032H/document

[42] T. J. Poinsot, S. Lele, Boundary conditions for direct simulations of compressible viscous flows, Journal of computational physics 101 (1) (1992) 104–129.

[43] R. Saurel, P. Boivin, O. Le Métayer, A general formulation for cavitating, boiling and evaporating flows, Computers & Fluids 128 (2016) 53–64.

[44] A. Chiapolino, P. Boivin, R. Saurel, A simple and fast phase transition relaxation solver for compressible multicomponent two-phase flows, Computers & Fluids 150 (2017) 31–45.

[45] B. E. Poling, J. M. Prausnitz, O. John Paul, R. C. Reid, The properties of gases and liquids, Vol. 5, Mcgraw-hill New York, 2001.

[46] R. Saurel, F. Petitpas, R. Abgrall, Modelling phase transition in metastable liquids: application to cavitating and flashing flows, Journal of Fluid Mechanics 607 (2008) 313–350.

[47] M. L. Michelsen, J. Mollerup, Thermodynamic Modelling: Fundamentals and Computational Aspects, Tie-Line Publications, 2004.

[48] H. Lund, A hierarchy of relaxation models for two-phase flow, SIAM Journal on Applied Mathematics 72 (6) (2012) 1713–1741.

[49] O. Colin, M. Rudgyard, Development of high-order Taylor–Galerkin schemes for LES, Journal of Computational Physics 162 (2) (2000) 338–371.

[50] C. Le Touze, Coupling between separated and dispersed two-phase flow models for the simulation of primary atomization in cryogenic combustion, Ph.D. thesis, Université Nice Sophia Antipolis (2015).
URL `https://tel.archives-ouvertes.fr/tel-01250527`

[51] T. Poinsot, D. Veynante, Theoretical and numerical combustion, RT Edwards, Inc., 2005.

[52] T. H. Chung, M. Ajlan, L. L. Lee, K. E. Starling, Generalized multiparameter correlation for nonpolar and polar fluid transport properties, Industrial & engineering chemistry research 27 (4) (1988) 671–679.

[53] P. Gaillard, Diffuse interfaces and LOx/H2 transcritical flames, Ph.D. thesis, Université Pierre et Marie Curie - Paris VI (Dec 2015).
URL https://tel.archives-ouvertes.fr/tel-01308564

[54] V. Giovangigli, Multicomponent flow modeling, Science China Mathematics 55 (2) (2012) 285–308.

[55] F. Nicoud, F. Ducros, Subgrid-scale stress modelling based on the square of the velocity gradient tensor, Flow, turbulence and Combustion 62 (3) (1999) 183–200.

[56] T. Schmitt, L. Selle, A. Ruiz, B. Cuenot, Large-eddy simulation of supercritical-pressure round jets, AIAA journal 48 (9) (2010) 2133–2144.

[57] D. K. Lilly, A proposed modification of the Germano subgrid-scale closure method, Physics of Fluids A: Fluid Dynamics 4 (3) (1992) 633–635.

[58] D. Veynante, L. Vervisch, Turbulent combustion modeling, Progress in energy and combustion science 28 (3) (2002) 193–266.

[59] P. Domingo, L. Vervisch, D. Veynante, Large-eddy simulation of a lifted methane jet flame in a vitiated coflow, Combustion and Flame 152 (3) (2008) 415–432.

[60] T. Schmitt, Y. Méry, M. Boileau, S. Candel, Large-eddy simulation of oxygen/methane flames under transcritical conditions, Proceedings of the Combustion Institute 33 (1) (2011) 1383–1390.

[61] C. Pera, O. Colin, S. Jay, Development of a FPI detailed chemistry tabulation methodology for internal combustion engines, Oil & Gas Science and Technology-Revue de l'IFP 64 (3) (2009) 243–258.

[62] L. Vingert, M. Habiballah, P. Vuillermoz, S. Zurbach, Mascotte, a test facility for cryogenic combustion research at high pressure, in: IAF, International Astronautical Congress, 51 st, Rio de Janeiro, Brazil, 2000.

[63] M. Habiballah, M. Orain, F. Grisch, L. Vingert, P. Gicquel, Experimental studies of high-pressure cryogenic flames on the Mascotte facility, Combustion Science and Technology 178 (1-3) (2006) 101–128.

[64] P. Schmitt, T. Poinsot, B. Schuermans, K. Geigle, Large-eddy simulation and experimental study of heat transfer, nitric oxide emissions and combustion instability in a swirled turbulent high-pressure burner, Journal of Fluid Mechanics 570 (2007) 17–46.

[65] R. H. Kraichnan, Diffusion by a random velocity field, The physics of fluids 13 (1) (1970) 22–31.

[66] A. Smirnov, S. Shi, I. Celik, Random flow generation technique for large eddy simulations and particle-dynamics modeling, Journal of fluids engineering 123 (2) (2001) 359–371.

[67] N. Chigier, R. D. Reitz, Regimes of jet breakup and breakup mechanisms-physical aspects, Recent advances in spray combustion: Spray atomization and drop burning phenomena. 1 (1996) 109–135.

[68] J. C. Lasheras, E. Hopfinger, Liquid jet instability and atomization in a coaxial gas stream, Annual review of fluid mechanics 32 (1) (2000) 275–308.

[69] A. Chiapolino, R. Saurel, B. Nkonga, Sharpening diffuse interfaces with compressible fluids on unstructured meshes, Journal of Computational Physics 340 (2017) 389–417.

[70] R. K. Shukla, C. Pantano, J. B. Freund, An interface capturing method for the simulation of multi-phase compressible flows, Journal of Computational Physics 229 (19) (2010) 7411–7439.